*J. metamorphic Geol.*, 2007, **25,** 225–243 doi:10.1111/j.1525-1314.2006.00686.x

# Ultrahigh-pressure metamorphism and exhumation of garnet-bearing ultramafic rocks from the Lanterman Range (northern Victoria Land, Antarctica)

R. PALMERI,[1] B. GHIRIBELLI,[1] G. RANALLI,[2] F. TALARICO[3] AND C. A. RICCI[1,3]
[1]*Museo Nazionale dell'Antartide, Università di Siena, via Laterina 8, 53100 Siena, Italy (palmerir@unisi.it)*
[2]*Department of Earth Sciences and Ottawa-Carleton Geoscience Centre, Carleton University, Ottawa, Canada K1S 5B6*
[3]*Dipartimento di Scienze della Terra, Università di Siena, via Laterina 8, 53100 Siena, Italy*

**ABSTRACT** Northern Victoria Land is a key area for the Ross Orogen – a Palaeozoic foldbelt formed at the palaeo-Pacific margin of Gondwana. A narrow and discontinuous high- to ultrahigh-pressure (UHP) belt, consisting of mafic and ultramafic rocks (including garnet-bearing types) within a metasedimentary sequence of gneisses and quartzites, is exposed at the Lanterman Range (northern Victoria Land). Garnet-bearing ultramafic rocks evolved through at least six metamorphic stages. Stage 1 is defined by medium-grained garnet + olivine + low-Al orthopyroxene + clinopyroxene, whereas finer-grained garnet + olivine + orthopyroxene + clinopyroxene + amphibole constitutes the stage 2 assemblage. Stage 3 is defined by kelyphites of orthopyroxene + clinopyroxene + spinel ± amphibole around garnet. Porphyroblasts of amphibole replacing garnet and clinopyroxene characterize stage 4. Retrograde stages 5 and 6 consist of tremolite + Mg-chlorite ± serpentine ± talc. A high-temperature (~950 °C), spinel-bearing protolith (stage 0), is identified on the basis of orthopyroxene + clinopyroxene + olivine + spinel + amphibole inclusions within stage 1 garnet. The *P–T* estimates for stage 1 are indicative of UHP conditions (3.2–3.3 GPa and 764–820 °C), whereas stage 2 is constrained between 726–788 °C and 2.6–2.9 GPa. Stage 3 records a decompression up to 1.1–1.3 GPa at 705–776 °C. Stages 4, 5 and 6 reflect uplift and cooling, the final estimates yielding values below 0.5 GPa at 300–400 °C. The retrograde *P–T* path is nearly isothermal from UHP conditions up to deep crustal levels, and becomes a cooling–unloading path from intermediate to shallow levels. The garnet-bearing ultramafic rocks originated in the mantle wedge and were probably incorporated into the subduction zone with felsic and mafic rocks with which they shared the subsequent metamorphic and geodynamic evolution. The density and rheology of the subducted rocks are compatible with detachment of slices along the subduction channel and gravity-driven exhumation.

**Key words:** Antarctica; exhumation; garnet-bearing ultramafic rocks; HP/UHP metamorphism; subduction.

## INTRODUCTION

Garnet-bearing ultramafic lenses are minor but important components of most high-pressure (HP) and UHP metamorphic terranes, and may provide information on the process of orogenesis and on crust–mantle interactions. Garnet-bearing ultramafic rocks emplaced into the continental crust of HP/UHP terranes have been classified into two broad categories (Brueckner & Medaris, 2000): crustal (category I) and mantle (category II) peridotites. The first type is considered to have formed in the lower crust, generally as layered mafic–ultramafic intrusions (Carswell *et al.*, 1983) or as serpentinized ophiolites (Evans & Trommsdorff, 1978) prior to subduction. Mantle peridotites may be derived: (i) from the mantle wedge above the underthrust continental crust which intruded the crust at shallow, intermediate or deep levels (Kalt *et al.*, 1995), (ii) from upwelling of the asthenosphere (Pearson *et al.*, 1995), or (iii) from old subcontinental lithosphere (Brueckner & Medaris, 1998). The study of garnet-bearing ultramafic rocks thus provides an important window into petrotectonic processes within the subcontinental mantle or the mantle wedge above the subducting slab (Liou & Carswell, 2000) and bears important geodynamic implications that are mostly obscure in other rock types (Tsai *et al.*, 2000).

The investigated ultramafic rocks in the Lanterman Range (northern Victoria Land, Antarctica) belong to the Gateway Hills Metamorphic Complex (Talarico *et al.*, 1998). The complex is part of the Ross Orogen, a foldbelt developed during the Early Palaeozoic as a consequence of the convergence between the Gondwana continental margin and the oceanic palaeo-Pacific plate.

This study focuses on microstructural, mineralogical and petrological features developed during the metamorphic peak and the subsequent retrograde evolution in garnet-bearing ultramafic rocks. In addition, the

© 2007 Blackwell Publishing Ltd 

medium-grained garnet contains mineral inclusions, which can be considered to record the initial stages of rock formation, i.e. prior to metamorphic peak.

Microstructural and petrological data, along with thermobarometric calculations applied to minerals assumed to represent thermodynamic equilibria, indicate that the peak conditions were realized under UHP metamorphic conditions. Indeed, in the Lanterman Range, on the basis of coesite relics, UHP metamorphism was reported for mafic rocks (Ghiribelli *et al.*, 2002), and a common tectono-metamorphic evolution between mafic and felsic host rocks, including the UHP metamorphic stage, was also described (Palmeri *et al.*, 2003).

The *P–T* evolution described for garnet-bearing ultramafic rocks is compared with those reconstructed for the associated mafic eclogites (Di Vincenzo *et al.*, 1997; Ghiribelli *et al.*, 2002) and quartzofeldspathic host gneisses (Palmeri *et al.*, 2003). All petrological features and rheological properties of the different rock units are considered and discussed for modelling the exhumation mechanism compatible with gravity-driven exhumation ('tectonic extrusion' *sensu* Ernst, 2001) along the subduction channel, and for defining a geodynamic scenario for this important part of the palaeo-Pacific margin of Gondwana.

## GEOLOGICAL SETTING

During the Late Precambrian to Early Palaeozoic, the palaeo-Pacific margin of Gondwana was involved in subduction-related orogenic activity which produced the Cambrian/Ordovician deformation, metamorphism and magmatism termed the Ross Orogeny in Antarctica (Kleinschmidt & Tessensohn, 1987; Borg & De Paolo, 1994; Ricci *et al.*, 1997). In northern Victoria Land, the Ross Orogen consists of three tectonometamorphic terranes (Bradshaw & Laird, 1983): the outboard Robertson Bay and Bowers Terranes and the inboard Wilson Terrane (Fig. 1a,b). The Wilson Terrane can be divided into an inner, low pressure (LP)–high temperature (HT) belt and an outer, narrow and discontinuous medium-pressure (MP) to high-pressure (HP) belt (Grew *et al.*, 1984) that comprises the eclogites of the Lanterman Range (Ricci *et al.*, 1996, 1997).

Three different lithotectonic units have been distinguished in the Lanterman Range (Talarico *et al.*, 1998) (Fig. 1c). From west to east they are: the Edixon Metamorphic Complex (EMC), the Bernstein Metamorphic Complex (BMC) and the Gateway Hills Metamorphic Complex (GHMC). The EMC mainly consists of a metasedimentary sequence which underwent medium- to high-grade metamorphism under prevailing low-pressure conditions. The BMC consists




**Fig. 1.** (a) Schematic map of Antarctica; (b) structural map of northern Victoria Land and main localities, and (c) geological map of the Lanterman Range (modified after Talarico *et al.*, 1998) with sample locations. RBT, Robertson Bay Terrane; BT, Bowers Terrane; WT, Wilson Terrane; LR, Lanterman Range.

© 2007 Blackwell Publishing Ltd

of micaschists and gneisses affected by medium- to high-grade metamorphism with an intermediate pressure character (Grew & Sandiford, 1984; Talarico *et al*., 1998). The GHMC is characterized by abundant mafic and ultramafic rocks, including well-preserved mafic eclogites (Ricci *et al*., 1996). The latter occur as lenses and pods (centimetres to metres in size) within a metasedimentary sequence represented by quartzofeldspathic gneisses and minor quartzites. The dominant structural element of the GHMC is a pervasive metamorphic foliation that strikes NW–SE and dips steeply to both the SW and NE, and which developed under amphibolite facies metamorphic conditions (Capponi *et al*., 1997; Talarico *et al*., 1998).

Ultramafic bodies (Kleinschmidt *et al*., 1987; Talarico *et al*., 1998) occur as lenses and pods (metres to tens of metres in size) within retrogressed mafic eclogites and/or quartzofeldspathic gneisses, with which they show concordant contacts. Ultramafic boudins have usually undergone intense retrogression and weathering, and consist mainly of serpentinized ultramafic rocks and minor amphibole ± magnesite ± talc fels (Capponi *et al*., 1997). Medium-grained amphibole-garnet fels occur throughout the GHMC as centimetre- to decimetre-thick layers. Well-preserved eclogite facies garnet-bearing ultramafic rocks are rare and were found 8 km north to north-east of Mt Bernstein, where they are associated with retrogressed mafic eclogites and mica-bearing gneisses. The locations of garnet-bearing ultramafic rocks described in this paper are indicated in Fig. 1.

## PETROGRAPHY

Two samples of ultramafic rocks were selected for this study: BC23, a well-preserved garnet-bearing ultramafic rock, and G12, an amphibole-garnet fels (lithological terms after Jackson, 1997). The two rocks were analysed in detail by optical and scanning electron microscopy (SEM) in order to decipher temporal relationships among the various minerals in different microstructural occurrences.

Sample BC23 is a well-preserved, inequigranular and slightly foliated garnet-bearing ultramafic rock. It shows a compositional–structural layering consisting of medium- to coarse-grained centimetric layers and fine-grained millimetric layers, which define a weak grain shape-preferred orientation fabric mainly because of pyroxene and amphibole crystals. The contact between the coarse- and fine-grained layers is highlighted by the development of porphyroblastic crystals of amphibole.

The medium- to coarse-grained layer mainly consists of relict garnet ($Grt_1$) porphyroblasts, olivine ($Ol_1$), together with platy porphyroblastic orthopyroxene ($Opx_1$) and very rare clinopyroxene ($Cpx_1$) (Fig. 2a–d). $Grt_1$ grains are large (up to 3 mm in size), anhedral and fractured (Fig. 2a–c). A peculiarity of $Grt_1$ is the presence of abundant tiny inclusions of $Opx_0$, $Cpx_0$, spinel ($Spl_0$), ilmenite ($Ilm_0$) and clinoamphibole ($Cam_0$) (Fig. 2a,b). Inclusions can be found as polycrystalline associations of $Cpx_0$, $Opx_0$, $Spl_0$ and $Cam_0$ or as single idioblastic crystals, especially $Cpx_0$ and $Cam_0$. $Ol_1$ forms anhedral and fractured porphyroblasts characterized by resorbed margins (Fig. 2c). Serpentine replacement is present along fractures. The contact between $Grt_1$ and $Ol_1$ is always characterized by 1- to 2-mm-wide cryptocrystalline kelyphitic coronas (Fig. 2c). $Opx_1$ (Fig. 2d) is elongated (up to 2 mm) and sheared, and it sometimes includes small (≤100 $\mu$m) idioblastic garnet, rounded olivine, clinopyroxene and ilmenite. Garnet enclosed in $Opx_1$ shows the same mineral inclusions found in porphyroblastic $Grt_1$. $Cpx_1$ is characterized by narrow crystals up to 1 cm long. $Opx_1$ and $Cpx_1$ are rarely in contact with each other, but both occur in contact with $Grt_1$.

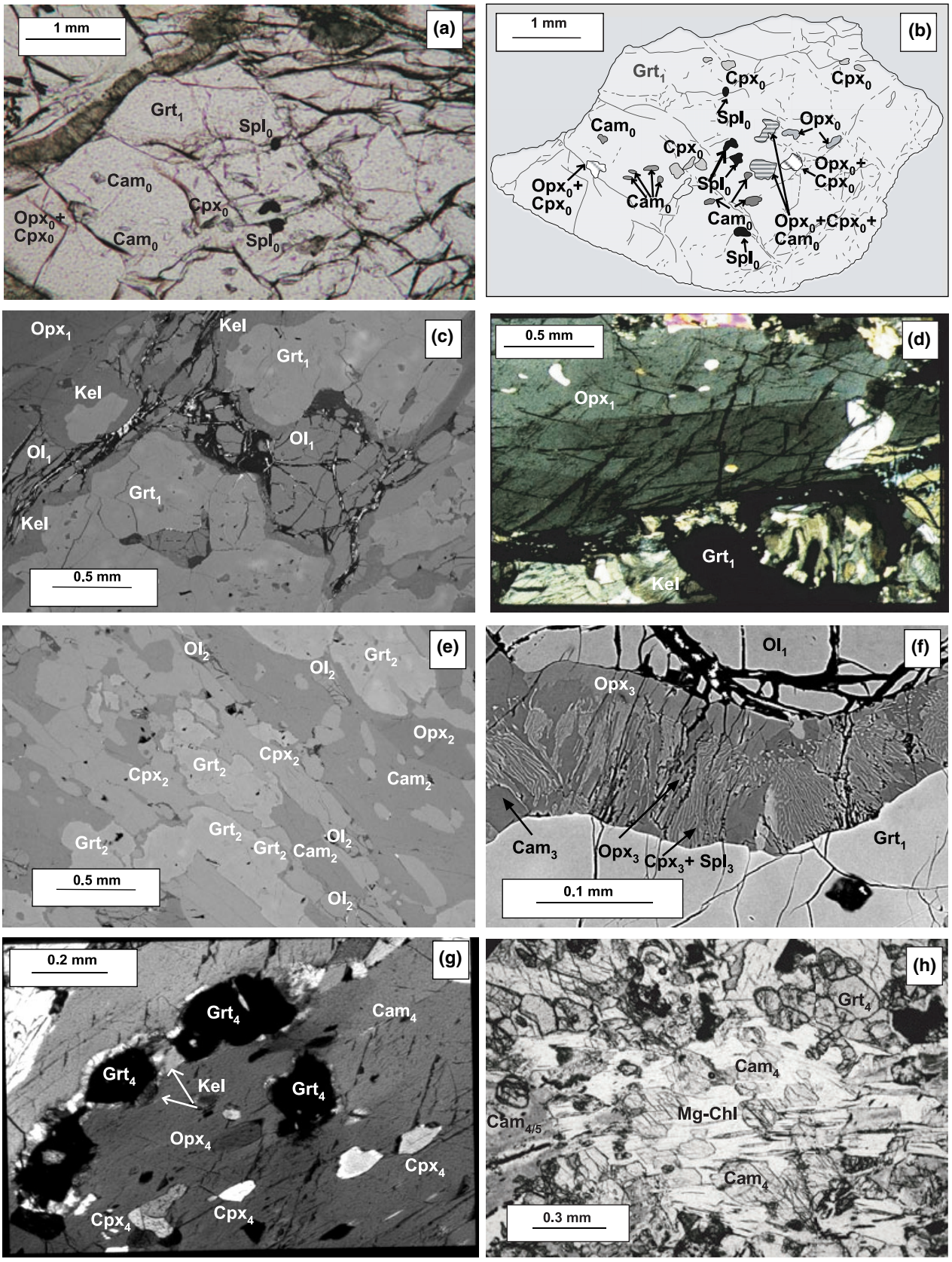
The fine-grained layer consists of dynamically recrystallized neoblasts of $Grt_2 + Cpx_2 + Opx_2 \pm Cam_2 \pm Ol_2$ (Fig. 2e). $Grt_2$ occurs as small (up to 300 $\mu$m) subidioblastic elongated grains; it is usually devoid of inclusions and has very tiny kelyphitic rims (Fig. 2e). $Opx_2$ (up to 1 mm in size) lacks inclusions and is less abundant than $Cpx_2$. Subidioblastic $Ol_2$ is present as small crystals and is devoid of kelyphitic rims. The presence of amphibole ($Cam_2$) in textural equilibrium with $Opx_2$ and $Cpx_2$ and with the crystallographic length of crystals oriented along the main anisotropy axis (Fig. 2e) is peculiar to this layer.

Of note are the kelyphitic coronas as revealed by SEM observations (Fig. 2f). They are composed of an inner zone consisting of anhedral $Opx_3 + Cpx_3 +$ vermicular $Spl_3 \pm Cam_3$ and an outer zone (usually in contact with $Ol_1$) mainly consisting of subidioblastic $Opx_3 \pm Cam_3$ (Fig. 2f). Vermicular spinel is radial and approximately normal to the garnet interface; the spinel-free portion of the kelyphitic rim is narrower than the spinel-bearing one. Only small resorbed garnet and/or olivine relics are present within well-developed, centimetric kelyphite.

The contact between medium- to coarse-grained and fine-grained layers is characterized by the development of large porphyroblastic crystals of amphibole ($Cam_4$) (up to 2–3 cm) containing resorbed garnet, anhedral grains of clinopyroxene, orthopyroxene and olivine, and portions of kelyphite (Fig. 2g). Green crystals of spinel ($Spl_4$) together with amphibole constitute pseudomorphs after garnet in the most retrogressed portions of the rock.

Sample G12, an amphibole-garnet fels characterized by a medium grain size, mainly consists of large (up to 3–4 cm) porphyroblastic crystals of amphibole ($Cam_4$) with no preferred orientation. Rare relics of small (≤100 $\mu$m) anhedral grains of garnet ($Grt_4$; Fig. 2g), sometimes preserving tiny kelyphitic rims, are present as inclusions in $Cam_4$. Resorbed clinopyroxene is present as minor relic inclusions in amphibole. Late fibrous amphibole ($Cam_5$) is present along fractures or along the cleavage of the poikiloblastic $Cam_4$. Mg-chlorite (Mg-Chl) (Fig. 2h) and rare talc (Tlc) are associated with $Cam_5$.

© 2007 Blackwell Publishing Ltd




© 2007 Blackwell Publishing Ltd

**Table 1.** Major and trace-element concentrations and CIPW normative mineralogy of samples BC23 and G12; sample PX (Fumagalli & Poli, 2005) is also reported for comparison.

| Samples | BC23 | G12 | PX |
|---|---|---|---|
| $SiO_2$ | 46.05 | 45.57 | 45.41 |
| $TiO_2$ | 0.13 | 0.15 | |
| $Al_2O_3$ | 10.92 | 10.00 | 8.26 |
| $Cr_2O_3$ | 0.38 | 0.33 | |
| $Fe_2O_3$ | 10.71 | 9.34 | |
| FeO | | | 9.81 |
| MnO | 0.16 | 0.14 | |
| MgO | 23.93 | 20.95 | 27.38 |
| NiO | 0.12 | 0.10 | |
| CaO | 7.01 | 8.02 | 8.32 |
| $Na_2O$ | 0.47 | 0.42 | 0.82 |
| $K_2O$ | < 0.03 | 0.15 | |
| $P_2O_5$ | Tr | 0.12 | |
| LOI | 0.84 | 4.85 | |
| Total | 100.7 | 100.10 | 100.00 |
| CIPW normative mineralogy | | | |
| Or | | 0.89 | |
| Ab | 3.98 | 3.55 | 6.94 |
| An | 27.69 | 24.96 | 18.80 |
| C | | | |
| Di | 5.63 | 11.16 | 17.71 |
| Hy | 28.84 | 31.47 | 7.36 |
| Ol | 29.30 | 19.15 | 45.56 |
| Mt | 3.68 | 2.93 | |
| Il | 0.25 | 0.28 | |
| Ap | | 0.28 | |
| Q | | | |
| Hm | | | |

Major elements determined by inductively coupled plasma (ICP)- emission spectrometry and trace elements by ICP-mass spectrometry at CRPG (Nancy, France).
LOI, loss on igniton all Fe reported as $Fe_2O_3$ and $FeO/FeO + Fe_2O_3 = 0.77$ for CIPW calculations (Le Maitre, 1976).

The bulk-rock chemical compositions of the two samples are reported in Table 1. Major- and trace-element contents and CIPW normative calculations indicate an olivine-websterite composition. The high anorthite content in normative plagioclase ($An_{87}$) and the lack of plagioclase among relic phases suggest that garnet-bearing ultramafic rocks developed from a plagioclase-free, spinel-bearing pyroxene to olivine-rich peridotitic protolith. Note that the composition of the analysed samples is very similar to the composition PX (Table 1), an olivine-poor garnet lherzolite approximating a Hawaiian peridotite nodule used in experiments by Fumagalli & Poli (2005). On the basis of the similar bulk chemical composition (Table 1) and of microstructural features such as the garnet and clinopyroxene relics within porphyroblastic amphibole, amphibole-garnet fels G12 is considered to be a retrogressed Grt-bearing ultramafic rock.

## MINERAL CHEMISTRY

Representative mineral analyses of samples BC23 and G12 are reported in Table 2(a–d). Mineral compositions were obtained using the JEOL JX 8600 electron microprobe fitted with four wavelength-dispersive spectrometers at the Istituto di Geoscienze e Georisorse (CNR, Firenze). Accelerating voltage was 15 kV and the sample current was 10 nA. Natural standards were used for calibration. Structural formulae were calculated on the basis of 12 oxygen for garnet, 6 for pyroxene, 4 for olivine and spinel, and 23 for amphibole. Ferrous and ferric iron contents were calculated by charge balance for garnet, pyroxene, olivine and spinel, and according to Holland & Blundy (1994) for amphibole. Leake *et al.* (1997) nomenclature was used for amphibole.

### Garnet

In sample BC23 garnet is always almandine/grossularite-rich pyrope in the different microtextural occurrences, whereas in amphibole-garnet fels G12, it is a pyrope/grossularite-rich almandine (Table 2a). In the Grs-Prp-Alm + Sps ternary diagram (Fig. 3), representative points of sample BC23 mainly plot within the A-type eclogite field (Coleman *et al.*, 1965), whereas representative points of G12 (where garnet is a resorbed relic within amphibole) mainly plot in the B-type field ($Grt_4$). However, some core compositions of sample G12 garnet plot in the A field. In sample BC23, no compositional differences were found between $Grt_1$ (relict porphyroblast) and garnet enclosed in porphyroblastic $Opx_1$. The garnet enclosed in $Opx_1$ is relatively homogeneous (analyses 1 & 2 in Table 2a and shaded area in Fig. 3) with no zoning, and may reflect a frozen equilibrium before or during the peak stage. On the contrary, relict porphyroblastic $Grt_1$ shows a slight zoning (Table 2a, analysis 3), with an increase in both $X_{Fe}$ (0.27–0.29) and $X_{Ca}$ (0.14–0.16) and a decrease in $X_{Mg}$ (0.58–0.54) from core to inner rim, and an opposite trend from inner to outer rim ($X_{Fe} = 0.26$; $X_{Ca} = 0.12$; $X_{Mg} = 0.58$). The Fe/Mg ratio is 0.48–0.53 from core to inner rim, and 0.45 at the outer rim.

Idioblastic garnet in the fine-grained layers ($Grt_2$) has a different and opposite zoning, with a slight increase in

**Fig. 2.** Photomicrographs and a drawing of microstructures of garnet-bearing ultramafic rocks. (a) Relict porphyroblastic garnet ($Grt_1$) with inclusions of dark spinel ($Spl_0$), clinopyroxene ($Cpx_0$), orthopyroxene ($Opx_0$) and amphibole ($Cam_0$). Plane polarized light, sample BC23. (b) Line drawing of relict porphyroblastic garnet ($Grt_1$) with mineral inclusions. Sample BC23. (c) Kelyphitic rims between porphyroblastic $Grt_1$ and olivine ($Ol_1$) in the medium-grained layer. Backscattered scanning electron microscope (BSE-SEM) image, sample BC23. (d) Porphyroblastic coarse-grained $Opx_1$ in the medium-grained layer. Crossed nicols, sample BC23. (e) Fine-grained layer with evident equilibrium among $Grt_2$, $Opx_2$, $Cpx_2$, $Cam_2$ and $Ol_2$. BSE-SEM image, sample BC23. (f) BSE image of the kelyphitic associations between $Grt_1$ and $Ol_1$, with an inner rim at the contact of garnet and an outer rim at the contact with olivine. Sample BC 23. (g) Porphyroblastic $Cam_4$ with $Cpx_4$ and $Grt_4$ inclusions. The latter shows a small kelyphitic rim. Crossed nicols, sample BC23. (h) $Cam_4$ with inclusions of $Grt_4$, partly replaced by tiny needles of the new $Cam_5$ and of Mg-chlorite (Mg-Chl). Plane polarized light, sample G12.

© 2007 Blackwell Publishing Ltd

**Table 2.** Selected electron microprobe analyses of (a) garnet, (b) pyroxene, (c) olivine and spinel, (d) amphibole.

| | Sample BC23 | | | | | | | | | | | | Sample G12 | |
|---|---|---|---|---|---|---|---|---|---|---|---|---|---|---|
| | 1 core | 1 rim | 2 core | 2 rim | 3 core | 3 inner rim | 3 rim | 4 core | 4 inner rim | 4 rim | 5 rim | 6 rim | 7 core | 8 rim |
| | $Grt_1$ in $Opx_1$ | | $Grt_1$ in $Opx_1$ | | $Grt_1$ porphyroblast | | | $Grt_2$ idioblast | | | $Grt_4$ relict | $Grt_4$ relict | $Grt_4$ relict | $Grt_4$ relict |
| (a) | | | | | | | | | | | | | | |
| $SiO_2$ | 41.49 | 41.17 | 41.29 | 41.43 | 41.57 | 41.19 | 41.42 | 41.26 | 41.36 | 40.99 | 41.24 | 41.48 | 39.80 | 39.37 |
| $TiO_2$ | 0.03 | bdl | 0.07 | 0.05 | 0.06 | bdl | 0.05 | 0.07 | 0.07 | 0.07 | 0.08 | bdl | 0.13 | 0.06 |
| $Al_2O_3$ | 22.72 | 22.87 | 22.58 | 23.00 | 23.08 | 22.70 | 22.38 | 22.50 | 22.72 | 22.02 | 23.20 | 23.45 | 22.31 | 22.36 |
| $Cr_2O_3$ | 0.48 | 0.59 | 0.4 | 0.71 | 0.42 | 0.47 | 1.07 | 0.66 | 0.53 | 1.12 | 0.51 | 0.13 | 0.58 | 0.70 |
| $FeO_{tot}$ | 13.73 | 13.96 | 13.44 | 13.41 | 13.57 | 14.21 | 13.81 | 15.78 | 14.22 | 14.92 | 14.20 | 13.92 | 21.30 | 20.21 |
| MnO | 0.38 | 0.40 | 0.42 | 0.32 | 0.35 | 0.41 | 0.37 | 0.48 | 0.37 | 0.40 | 0.38 | 0.48 | 0.58 | 1.10 |
| MgO | 16.35 | 16.31 | 15.53 | 16.31 | 16.12 | 15.04 | 16.34 | 14.29 | 16.14 | 14.68 | 15.33 | 17.22 | 7.77 | 8.05 |
| CaO | 5.55 | 5.31 | 6.31 | 5.66 | 5.59 | 6.11 | 5.39 | 5.51 | 5.28 | 5.85 | 5.77 | 4.42 | 9.35 | 9.12 |
| Total | 100.73 | 100.61 | 100.04 | 100.89 | 100.76 | 100.13 | 100.83 | 100.55 | 100.69 | 100.05 | 100.71 | 101.10 | 101.82 | 100.97 |
| Si | 2.996 | 2.978 | 3.010 | 2.990 | 3.001 | 3.009 | 2.994 | 3.019 | 2.993 | 3.012 | 2.991 | 2.980 | 2.986 | 2.975 |
| Al | 1.934 | 1.950 | 1.940 | 1.956 | 1.964 | 1.955 | 1.907 | 1.941 | 1.939 | 1.907 | 1.984 | 1.985 | 1.973 | 1.991 |
| Ti | 0.002 | | 0.004 | 0.003 | 0.003 | | 0.003 | 0.004 | 0.004 | 0.004 | 0.004 | | 0.007 | 0.003 |
| Cr | 0.027 | 0.034 | 0.023 | 0.040 | 0.024 | 0.027 | 0.061 | 0.038 | 0.030 | 0.065 | 0.029 | 0.007 | 0.030 | 0.042 |
| $Fe^{3+}$ | 0.044 | 0.061 | 0.020 | 0.030 | 0.003 | 0.000 | 0.039 | 0.000 | 0.037 | 0.000 | 0.000 | 0.070 | 0.000 | 0.020 |
| $Fe^{2+}$ | 0.785 | 0.784 | 0.799 | 0.779 | 0.816 | 0.868 | 0.796 | 0.966 | 0.824 | 0.917 | 0.861 | 0.766 | 1.337 | 1.257 |
| Mn | 0.023 | 0.025 | 0.026 | 0.019 | 0.021 | 0.025 | 0.023 | 0.030 | 0.023 | 0.025 | 0.023 | 0.029 | 0.037 | 0.071 |
| Mg | 1.759 | 1.758 | 1.679 | 1.754 | 1.734 | 1.637 | 1.760 | 1.558 | 1.741 | 1.607 | 1.657 | 1.844 | 0.869 | 0.907 |
| Ca | 0.430 | 0.412 | 0.493 | 0.437 | 0.433 | 0.479 | 0.418 | 0.432 | 0.410 | 0.461 | 0.449 | 0.340 | 0.752 | 0.738 |
| Total | 8.000 | 8.002 | 7.994 | 8.008 | 7.999 | 8.000 | 8.001 | 7.988 | 8.001 | 7.998 | 7.998 | 8.021 | 7.991 | 8.004 |

| | Sample BC23 | | | | | | | | | | | | | |
|---|---|---|---|---|---|---|---|---|---|---|---|---|---|---|
| | *Orthopyroxene* | | | | | | | | *Clinopyroxene* | | | | | |
| | 1 | 2 | 3 core | 3 rim | 4 core | 5 core | 6 | 7 | 1 | 2 | 3 | 4 | 5 | 6 |
| | $Opx_0$ in $Grt_1$ | $Opx_0$ in $Grt_1$ | $Opx_1$ porphyroblast | | $Opx_1$ porphyroblast | $Opx_2$ idioblast | $Opx_{3a}$ kelyphite | $Opx_{3b}$ kelyphite | $Cpx_0$ in $Grt_1$ | $Cpx_0$ in $Grt_1$ | $Cpx_1$ porphyroblast | $Cpx_2$ idioblast | $Cpx_2$ idioblast | $Cpx_3$ kelyphite |
| (b) | | | | | | | | | | | | | | |
| $SiO_2$ | 55.51 | 55.24 | 57.44 | 57.13 | 57.22 | 57.08 | 56.03 | 55.12 | 53.56 | 54.33 | 54.59 | 54.30 | 55.17 | 53.27 |
| $TiO_2$ | bdl | 0.02 | 0.08 | 0.07 | 0.07 | bdl | 0.02 | bdl | 0.06 | 0.06 | 0.04 | 0.05 | 0.06 | 0.11 |
| $Al_2O_3$ | 3.06 | 2.98 | 0.78 | 0.63 | 0.44 | 0.61 | 1.18 | 3.30 | 2.39 | 1.18 | 1.30 | 0.87 | 1.14 | 1.75 |
| $Cr_2O_3$ | 0.08 | 0.06 | bdl | 0.03 | 0.00 | 0.05 | 0.10 | 0.10 | 0.05 | 0.11 | 0.16 | 0.23 | 0.23 | 0.13 |
| $FeO_{tot}$ | 10.01 | 10.68 | 8.78 | 9.31 | 7.95 | 8.08 | 9.92 | 10.9 | 2.79 | 2.93 | 2.91 | 2.24 | 2.66 | 2.71 |
| MnO | 0.15 | bdl | 0.06 | 0.11 | 0.09 | 0.12 | 0.10 | 0.16 | 0.02 | 0.09 | 0.00 | 0.04 | 0.03 | 0.08 |
| MgO | 31.16 | 31.29 | 33.74 | 33.58 | 33.51 | 33.60 | 31.54 | 30.89 | 16.61 | 17.35 | 16.65 | 17.16 | 17.04 | 16.87 |
| CaO | 0.92 | 0.19 | 0.22 | 0.19 | 0.19 | 0.20 | 0.27 | 0.31 | 24.22 | 24.13 | 23.13 | 23.83 | 23.11 | 24.37 |
| $Na_2O$ | 0.03 | bdl | 0.08 | 0.10 | bdl | 0.03 | bdl | bdl | 0.09 | 0.57 | 0.61 | 0.37 | 0.73 | 0.03 |
| $K_2O$ | 0.02 | 0.00 | 0.00 | 0.00 | 0.00 | 0.02 | 0.00 | 0.00 | 0.00 | 0.00 | 0.00 | 0.04 | 0.00 | 0.00 |
| Total | 100.94 | 100.46 | 101.18 | 101.15 | 99.47 | 99.79 | 99.16 | 100.78 | 99.79 | 100.75 | 99.39 | 99.13 | 100.17 | 99.32 |
| Si | 1.930 | 1.926 | 1.972 | 1.965 | 1.994 | 1.984 | 1.978 | 1.920 | 1.952 | 1.958 | 1.993 | 1.987 | 1.996 | 1.952 |
| Al | 0.130 | 0.123 | 0.032 | 0.026 | 0.018 | 0.025 | 0.049 | 0.140 | 0.103 | 0.05 | 0.056 | 0.038 | 0.049 | 0.076 |
| Ti | | 0.001 | 0.002 | 0.002 | 0.002 | | 0.001 | | 0.002 | 0.002 | 0.001 | 0.001 | 0.002 | 0.003 |
| Cr | 0.002 | 0.002 | | 0.001 | 0.000 | 0.001 | 0.003 | 0.003 | 0.001 | 0.003 | 0.005 | 0.007 | 0.007 | 0.004 |
| $Fe^{3+}$ | 0.010 | 0.022 | 0.025 | 0.046 | 0.000 | 0.008 | 0.000 | 0.020 | 0.000 | 0.067 | 0.000 | 0.008 | 0.001 | 0.013 |
| $Fe^{2+}$ | 0.280 | 0.289 | 0.227 | 0.222 | 0.232 | 0.227 | 0.293 | 0.300 | 0.085 | 0.014 | 0.089 | 0.061 | 0.080 | 0.070 |
| Mn | 0.004 | 0.004 | 0.002 | 0.003 | 0.003 | 0.004 | 0.003 | 0.005 | 0.001 | 0.003 | 0.000 | 0.001 | 0.001 | 0.002 |
| Mg | 1.620 | 1.626 | 1.727 | 1.722 | 1.740 | 1.741 | 1.659 | 1.610 | 0.902 | 0.932 | 0.906 | 0.936 | 0.919 | 0.921 |
| Ca | 0.030 | 0.007 | 0.008 | 0.007 | 0.007 | 0.007 | 0.010 | 0.010 | 0.946 | 0.932 | 0.905 | 0.934 | 0.896 | 0.957 |
| Na | 0.002 | | 0.005 | 0.007 | | 0.002 | | | 0.006 | 0.040 | 0.043 | 0.026 | 0.051 | 0.002 |
| K | 0.001 | 0.000 | 0.000 | 0.000 | 0.000 | 0.001 | 0.000 | 0.000 | 0.000 | 0.000 | 0.000 | 0.002 | 0.000 | 0.000 |
| Total | 4.009 | 4.000 | 4.000 | 4.001 | 3.996 | 4.000 | 3.996 | 4.008 | 3.998 | 4.001 | 3.998 | 4.001 | 4.002 | 4.000 |

| | *Olivine* | | | | *Spinel* | | | | |
|---|---|---|---|---|---|---|---|---|---|
| | 1 | 2 core | 2 rim | 3 core | 1 | 2 | 3 | 4 | 5 |
| | $Ol_0$ in $Grt_1$ | $Ol_1$ porphyroblast | | $Ol_2$ idioblast | $Spl_0$ in Grt1 | $Spl_0$ in $Grt_1$ | $Spl_3$ kelyphite | $Spl_3$ kelyphite | $Spl_4$ *after Grt* |
| (c) | | | | | | | | | |
| $SiO_2$ | 40.40 | 40.25 | 39.29 | 39.57 | 0.07 | 0.20 | 0.00 | 0.00 | 0.06 |
| $TiO_2$ | 0.00 | 0.03 | 0.00 | 0.00 | 0.39 | 0.00 | 0.00 | 0.00 | 0.05 |
| $Al_2O_3$ | 0.00 | 0.04 | 0.00 | 0.00 | 60.72 | 64.1 | 53.94 | 38.86 | 61.47 |

© 2007 Blackwell Publishing Ltd

**Table 2.** (*Cont'd*)

| | *Olivine* | | | | *Spinel* | | | | |
|---|---|---|---|---|---|---|---|---|---|
| | 1 | 2 core | 2 rim | 3 core | 1 | 2 | 3 | 4 | 5 |
| | $Ol_0$ in $Grt_1$ | $Ol_1$ porphyroblast | | $Ol_2$ idioblast | $Spl_0$ in Grt1 | $Spl_0$ in $Grt_1$ | $Spl_3$ kelyphite | $Spl_3$ kelyphite | $Spl_4$ *after Grt* |
| $Cr_2O_3$ | 0.00 | 0.00 | 0.00 | 0.00 | 7.57 | 5.50 | 2.87 | 1.26 | 2.82 |
| $FeO_{tot}$ | 12.54 | 15.34 | 15.32 | 14.80 | 10.72 | 10.57 | 12.78 | 11.25 | 21.25 |
| MnO | 0.00 | 0.15 | 0.12 | 0.14 | 0.08 | 0.1 | 0.06 | 0.09 | 0.21 |
| MgO | 47.43 | 44.24 | 45.11 | 44.61 | 20.17 | 20.33 | 20.88 | 24.89 | 12.47 |
| CaO | 0.00 | 0.02 | 0.00 | 0.01 | 0.09 | 0.13 | 0.06 | 0.16 | 0.02 |
| Total | 100.37 | 100.07 | 99.84 | 99.13 | 99.81 | 100.93 | 99.93 | 101.66 | 98.35 |
| Si | 0.996 | 1.009 | 0.986 | 1.001 | 0.002 | 0.005 | 0.000 | 0.000 | 0.002 |
| Al | 0.000 | 0.001 | 0.000 | 0.000 | 1.832 | 1.894 | 1.596 | 1.096 | 1.948 |
| Ti | 0.000 | 0.001 | 0.000 | 0.000 | 0.008 | 0.000 | 0.000 | 0.000 | 0.001 |
| Cr | 0.000 | 0.000 | 0.000 | 0.000 | 0.153 | 0.109 | 0.057 | 0.024 | 0.060 |
| $Fe^{3+}$ | 0.000 | 0.000 | 0.026 | 0.000 | 0.000 | 0.000 | 0.000 | 0.000 | 0.000 |
| $Fe^{2+}$ | 0.259 | 0.322 | 0.296 | 0.313 | 0.229 | 0.221 | 0.268 | 0.225 | 0.478 |
| Mn | 0.000 | 0.003 | 0.003 | 0.003 | 0.002 | 0.002 | 0.001 | 0.002 | 0.005 |
| Mg | 1.743 | 1.653 | 1.690 | 1.682 | 0.769 | 0.759 | 0.781 | 0.887 | 0.500 |
| Ca | 0.000 | 0.001 | 0.000 | 0.000 | 0.002 | 0.003 | 0.002 | 0.004 | 0.001 |
| Total | 2.998 | 2.990 | 3.001 | 2.999 | 2.997 | 2.993 | 2.939 | 2.839 | 2.995 |

| | Sample BC23 | | | | | | | | | Sample G12 | |
|---|---|---|---|---|---|---|---|---|---|---|---|
| | 1 | 2 | 3 | 4 | 5 | 6 | 7 core | 7 rim | 8 core | 1 | 2 |
| | $Cam_0$ in $Grt_1$ | $Cam_0$ in $Grt_1$ | $Cam_2$ nematoblast | $Cam_2$ nematoblast | $Cam_3$ kelyphite | $Cam_3$ kelyphite | $Cam_4$ porphyroblast | $Cam_4$ porphyroblast | $Cam_4$ porphyroblast | $Cam_5$ fibrous | $Cam_5$ fibrous |
| (d) | | | | | | | | | | | |
| $SiO_2$ | 45.57 | 45.78 | 46.67 | 44.28 | 46.78 | 46.85 | 47.03 | 46.07 | 47.63 | 52.73 | 56.20 |
| $TiO_2$ | 0.70 | 0.73 | 0.34 | 0.07 | 0.36 | 0.37 | 0.34 | 0.39 | 0.36 | 0.13 | 0.00 |
| $Al_2O_3$ | 13.88 | 13.68 | 11.64 | 15.85 | 12.74 | 10.67 | 10.77 | 11.86 | 10.55 | 6.44 | 3.48 |
| $Cr_2O_3$ | 0.86 | 0.76 | 1.03 | 0.51 | 0.30 | 0.43 | 0.44 | 0.66 | 0.24 | 0.00 | 0.00 |
| $FeO_{tot}$ | 3.80 | 4.09 | 4.26 | 4.50 | 3.69 | 4.64 | 4.10 | 4.20 | 4.39 | 3.74 | 4.31 |
| MnO | 0.03 | 0.00 | 0.11 | 0.05 | 0.05 | 0.06 | 0.00 | 0.02 | 0.00 | 0.00 | 0.00 |
| MgO | 17.97 | 17.81 | 18.39 | 16.90 | 18.44 | 19.21 | 19.47 | 18.62 | 19.41 | 20.63 | 20.86 |
| CaO | 12.86 | 12.70 | 11.82 | 12.02 | 12.82 | 11.63 | 11.82 | 11.59 | 11.79 | 12.51 | 11.88 |
| $Na_2O$ | 1.88 | 2.23 | 2.05 | 2.61 | 2.33 | 2.38 | 2.39 | 2.43 | 2.40 | 0.84 | 0.37 |
| $K_2O$ | 0.12 | 0.09 | 0.64 | 0.02 | 0.00 | 0.33 | 0.57 | 0.46 | 0.50 | 0.00 | 0.14 |
| Total | 97.67 | 97.87 | 96.95 | 96.81 | 97.51 | 96.57 | 96.93 | 96.30 | 97.27 | 97.02 | 97.24 |
| Si | 6.389 | 6.424 | 6.599 | 6.263 | 6.565 | 6.657 | 6.645 | 6.553 | 6.699 | 7.310 | 7.767 |
| Al | 2.294 | 2.263 | 1.940 | 2.643 | 2.108 | 1.787 | 1.794 | 1.989 | 1.749 | 1.052 | 0.567 |
| Ti | 0.074 | 0.077 | 0.036 | 0.007 | 0.038 | 0.040 | 0.036 | 0.042 | 0.038 | 0.014 | 0.000 |
| Cr | 0.095 | 0.084 | 0.115 | 0.057 | 0.033 | 0.048 | 0.049 | 0.074 | 0.027 | 0.000 | 0.000 |
| $Fe^{3+}$ | 0.229 | 0.133 | 0.250 | 0.252 | 0.103 | 0.259 | 0.241 | 0.248 | 0.257 | 0.216 | 0.000 |
| $Fe^{2+}$ | 0.191 | 0.332 | 0.253 | 0.281 | 0.318 | 0.262 | 0.244 | 0.251 | 0.260 | 0.218 | 0.498 |
| Mn | 0.004 | 0.000 | 0.013 | 0.006 | 0.006 | 0.007 | 0.000 | 0.002 | 0.000 | 0.000 | 0.000 |
| Mg | 3.755 | 3.725 | 3.875 | 3.563 | 3.857 | 4.068 | 4.100 | 3.947 | 4.068 | 4.262 | 4.296 |
| Ca | 1.932 | 1.910 | 1.791 | 1.822 | 1.928 | 1.771 | 1.789 | 1.766 | 1.777 | 1.858 | 1.759 |
| Na | 0.511 | 0.607 | 0.562 | 0.716 | 0.635 | 0.656 | 0.655 | 0.670 | 0.655 | 0.226 | 0.099 |
| K | 0.021 | 0.016 | 0.116 | 0.004 | 0.000 | 0.060 | 0.103 | 0.084 | 0.090 | 0.000 | 0.025 |
| Total | 15.495 | 15.571 | 15.550 | 15.614 | 15.591 | 15.615 | 15.656 | 15.626 | 15.620 | 15.599 | 15.011 |

bdl: below detected limit.

pyrope ($X_{Mg} = 0.52$–$0.57$) and a decrease in almandine ($X_{Fe} = 0.32$–$0.27$) and grossularite ($X_{Ca} = 0.14$–$0.12$) from core to inner rim, and an opposite trend from inner to outer rim ($X_{Mg} = 0.53$; $X_{Fe} = 0.30$; $X_{Ca} = 0.15$) (Table 2a, analyses 4). The Fe/Mg ratio is 0.62–0.49 from core to inner rim, and ~0.57 at the outer rim. The $Cr_2O_3$ content is low (0.4–1.12 wt%), with the highest values corresponding to $Grt_2$ rims.

## Orthopyroxene

Orthopyroxene was analysed only in sample BC23 (Table 2b). It is rich in the enstatite component (83–89%), with lower values ($En_{83}$%) corresponding to orthopyroxene ($Opx_0$) enclosed in $Grt_1$ or in kelyphite ($Opx_3$), and higher values ($En_{89}$%) corresponding to porphyroblastic $Opx_1$. Different $Al_2O_3$ contents were detected in orthopyroxene from different microstructural settings. $Opx_1$ shows the lowest $Al_2O_3$ content (0.44–0.78 wt%). A slight decrease from core to rim (0.78–0.63 wt%) was sometimes observed in $Opx_1$ at the contact with $Grt_1$. Relic orthopyroxene in $Grt_1$ shows higher $Al_2O_3$ content (up to 3.06 wt%), and orthopyroxene within kelyphitic rims shows comparable values ($Al_2O_3$ up to 3.3 wt%). The latter value is found in $Opx_3$ of outer kelyphitic rims ($Opx_{3b}$ in

© 2007 Blackwell Publishing Ltd

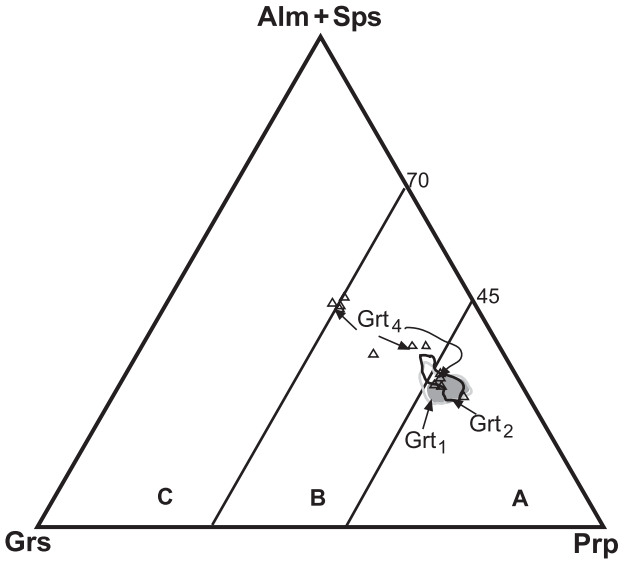



**Fig. 3.** Garnet ternary diagram after Coleman *et al.* (1965). End-members are almandine + spessartine (Alm + Sps), grossularite (Grs) and pyrope (Prp). Fields A, B and C represent the compositional variations of garnet in eclogites associated with kimberlites and peridotites (A), gneiss (B) and blueschist (C). $Grt_1$ and $Grt_2$ overlap in the figure. The gray area represents the composition of $Grt_1$ enclosed in $Opx_1$. Representative points in the B field of $Grt_1$ and $Grt_2$ correspond to rim compositions. Triangles refer to the most retrogressed $Grt_4$ usually found as inclusions in $Cam_4$. Note that some $Grt_4$ data points are in the A field and overlap with those of $Grt_1$ and $Grt_2$, while others lie between fields B and C. The former are core compositions and the latter are rim compositions.

Table 2b), whereas lower values ($Al_2O_3$ up to 1.18 wt%) were found in inner kelyphitic rims ($Opx_{3a}$ in Table 2b). The $Al_2O_3$ content in idioblastic $Opx_2$ from the fine-grained layer is comparable with that in porphyroblastic rims (0.61 wt%). $Cr_2O_3$ contents reach 0.15 wt% and are usually lower than that in clinopyroxene.

### Clinopyroxene

Clinopyroxene was analysed only in sample BC23 (Table 2b). It is diopsidic, with $X_{Mg}$ ranging from 0.91 to 0.96 and with a jadeite content from 0 to 5.0 mol.%; the highest $X_{Mg}$ and the lowest jadeite values refer to clinopyroxene ($Cpx_0$) enclosed in porphyroblastic $Opx_1$. The highest jadeite content (5 mol.%) is found in $Cpx_2$ in the fine-grained layer. $Cr_2O_3$ and $Na_2O$ contents are variable: $Cr_2O_3$ ranges from 0 to 0.44 wt%, and $Na_2O$ from 0.03 to 0.82 wt%. The lowest values usually refer to clinopyroxene in kelyphitic rims ($Cpx_3$), and the highest to $Cpx_2$ in the fine-grained layer. $Al_2O_3$ is variable, with the highest value (2.39%) reported for polycrystalline inclusions ($Cpx_0$) in $Grt_1$, and the lowest (0.87%) for $Cpx_2$ in the fine-grained layer.

### Olivine

$Ol_1$ and $Ol_2$ are homogeneous and show a very limited compositional range (Table 2c), with $X_{Mg}$ ranging from 0.84 to 0.86; olivine enclosed in $Opx_1$ or $Grt_1$ ($Ol_0$) has a slightly higher Mg content ($X_{Mg} = 0.87$).

### Spinel

Spinel ($Spl_0$) enclosed in $Grt_1$ and that found in kelyphite ($Spl_3$) are compositionally chromium-bearing pleonaste (Table 2c), with a $Cr_2O_3$ content of up to 7.57 wt% for $Spl_0$ within $Grt_1$ and up to 2.87 wt% in the kelyphite ($Spl_3$); $X_{Mg}$ varies from 0.72 to 0.80 for both types, with the highest values mainly found in spinel within garnet. Green spinel ($Spl_4$) in pseudomorphs after garnet is picotite and shows the lowest $X_{Mg}$ value (0.51), with $Cr_2O_3$ contents comparable with those of spinel in kelyphites.

### Amphibole

Analyses are reported in Table 2d. Early amphibole inclusions ($Cam_0$) in porphyroblastic $Grt_1$ are mainly Mg-hornblende, pargasite and very rarely tschermakite with very low $K_2O$ (0.01–0.06 wt%) and low $Na_2O$ (1.16–2.1 wt%) contents. Idioblastic amphibole ($Cam_2$) in equilibrium with pyroxene, garnet and olivine in the fine-grained layer is mainly edenite and Mg-hornblende. $K_2O$ (0.44–0.66 wt%) and $Na_2O$ (2.05–2.73 wt%) contents are higher than in the amphibole enclosed in $Grt_1$. Amphibole in kelyphite ($Cam_3$) is edenite or Mg-hornblende, with very low $K_2O$ (up to 0.02 wt%) and low $Na_2O$ (1.35–2.33 wt%). Poikiloblastic amphibole ($Cam_4$) is edenite, Mg-hornblende and pargasite, with $K_2O$ (0.41–0.73 wt%) and $Na_2O$ (1.94–2.77 wt%) contents comparable with those in the fine-grained layers. The very late amphibole needles are tremolitic in composition ($Cam_5$). In an $Al^{VI}$ *v.* $Al^{IV}$ plot (Fig. 4a), amphibole ($Cam_0$) enclosed in $Grt_1$ and that in kelyphite ($Cam_3$), together with the Al-richest amphibole in the fine-grained layers ($Cam_2$), describe a linear trend subparallel to the tremolite-pargasite line (slope of 2). The poikiloblastic amphibole ($Cam_4$) and Al-poor amphibole in the fine-grained layers ($Cam_2$) cluster in an area between the edenite and pargasite end-members. Late amphibole ($Cam_5$) plots near the tremolite end-member (Fig. 4). A variation in A site occupancy with $Al^{IV}$ (edenite substitution) for amphibole ($Cam_0$) within $Grt_1$ and for a few $Cam_2$ amphibole in the fine-grained layers is shown in Fig. 4(b), whereas late tremolite ($Cam_5$) is subparallel to the hornblende-tremolite line. Amphibole in kelyphite ($Cam_3$), porphyroblasts ($Cam_4$) and the remaining amphibole in the fine-grained layers ($Cam_2$) plot between the pargasite-tremolite and hornblende-tremolite joins. Figure 4 suggests that the pargasite substitution [$\square$ (A) + $Mg^{VI}$ + 2 $Si^{IV}$ = Na (A) + $Al^{VI}$ + $2Al^{IV}$]

© 2007 Blackwell Publishing Ltd

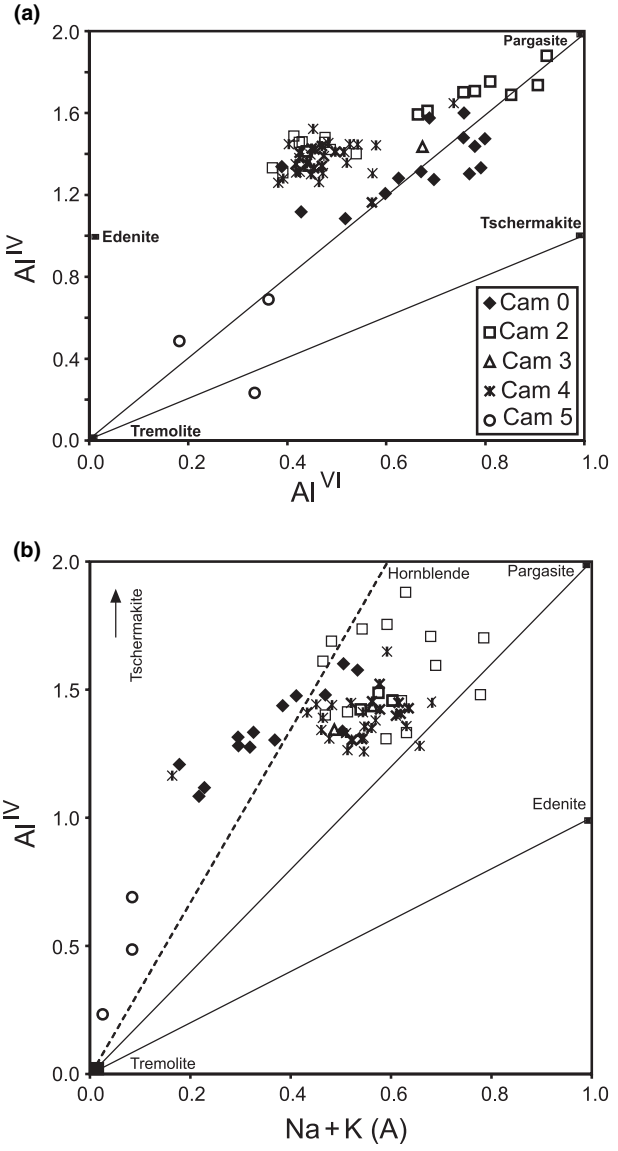



**Fig. 4.** Plots (Spear, 1981) of amphibole compositions. (a) $Al^{IV}$ *v.* $Al^{VI}$; (b) $Al^{IV}$ *v.* the A site occupancy for amphibole from the different microstructural settings.

occurred and can be ascribed to the coupled tschermakite ($2Si^{IV} + 2Mg^{VI} = 2Al^{IV} + 2Al^{VI}$) and edenite [$\square$ (A) + $Si^{IV} = Na(A) + Al^{IV}$] substitutions.

The trends suggest that their different microstructural occurrences are linked to different stages of equilibration of the rock. An early stage of crystallization ($Cam_0$), probably at high temperatures, is followed by four different stages represented by $Cam_2$ amphibole generally showing the highest aluminium contents, by a few amphibole in kelyphite ($Cam_3$) compositionally similar to early $Cam_0$, by porphyroblastic crystals ($Cam_4$) generally showing the lowest aluminium contents, and by late tremolite ($Cam_5$).

## METAMORPHIC EVOLUTION

The mineral chemistry and microstructural features indicate that garnet-bearing ultramafic rocks and amphibole-garnet fels of the Lanterman Range record multistage equilibria. At least six metamorphic stages occurred after the formation of the spinel-bearing protolith (Table 3; Fig. 5).

### Description of stages

#### *Stage 0 – spinel-bearing protolith*

The abundant inclusions of $Cpx_0$, $Opx_0$, $Spl_0$, $Cam_0$, $Ilm_0$ and $Ol_0$ (Table 3; Fig. 5) found in porphyroblastic $Grt_1$ and within garnet enclosed in porphyroblastic $Opx_1$ can be considered relics of the protolith rock. Assuming that these inclusions represent an equilibrium assemblage, the protolith could be either a spinel-bearing igneous pyroxenite or a pyroxene-rich spinel-bearing granulite derived from an ultramafic igneous protolith.

#### *Stage 1 – eclogite facies (medium-grained)*

The medium-grained porphyroblastic assemblage $Grt_1$, $Opx_1$, $Cpx_1$, $Ol_1$ (Fig. 5; Table 3) represents an eclogite facies stage which developed from the early assemblage through the reaction of spinel with orthopyroxene and clinopyroxene to form garnet and olivine (R1 reaction) (Obata & Thompson, 1981) and from the breakdown of amphibole to form garnet, pyroxene and olivine (R2 reaction) (Niida & Green, 1999):

$$Opx_0 + Cpx_0 + Spl_0 = Grt_1 + Ol_1 \qquad (R1)$$

$$Cam_0 = Cpx_1 + Grt_1 + Opx_1 + Ol_1 + H_2O. \qquad (R2)$$

**Table 3.** Metamorphic evolution of garnet-bearing ultramafic rocks.

| Stage | Mineral assemblage | Occurrence | Interpretation |
|---|---|---|---|
| 0 | $Opx_0 + Cpx_0 + Ol_0 + Spl_0 + Cam_0$ | Inclusions in $Grt_1$ of sample BC23. | High-*T* protolith |
| 1 | $Opx_1 + Cpx_1 + Ol_1 + Grt_1$ | Medium-grained layer of sample BC23. | Eclogite facies |
| 2 | $Opx_2 + Cpx_2 + Ol_2 + Grt_2 + Cam_2$ | Fine-grained layer of sample BC23. | Eclogite facies |
| 3 | $Opx_3 + Cpx_3 + Spl_3 +$ rim $Grt_1 \pm Cam_3$ | Kelyphite of sample BC23. | Granulite/HP–HT amphibolite facies |
| 4 | $Cam_4 \pm Spl_4 \pm Grt_4 \pm Cpx_4 \pm Opx_4$ | Between medium and fine-grained layers of sample BC23 or the main part of fels G12. | HT-Medium *P* amphibolite facies |
| 5 | $Cam_5 \pm Chl_5$ | Along cleavages of porphyroblasts $Cam_4$ of fels G12. | Low *T*-low *P* amphibolite facies |
| 6 | $Chl_6 \pm Srp_6 \pm Tlc_6 \pm Cam_6$ | Retrogressed portions of fels G12 | Greenschist facies |

© 2007 Blackwell Publishing Ltd

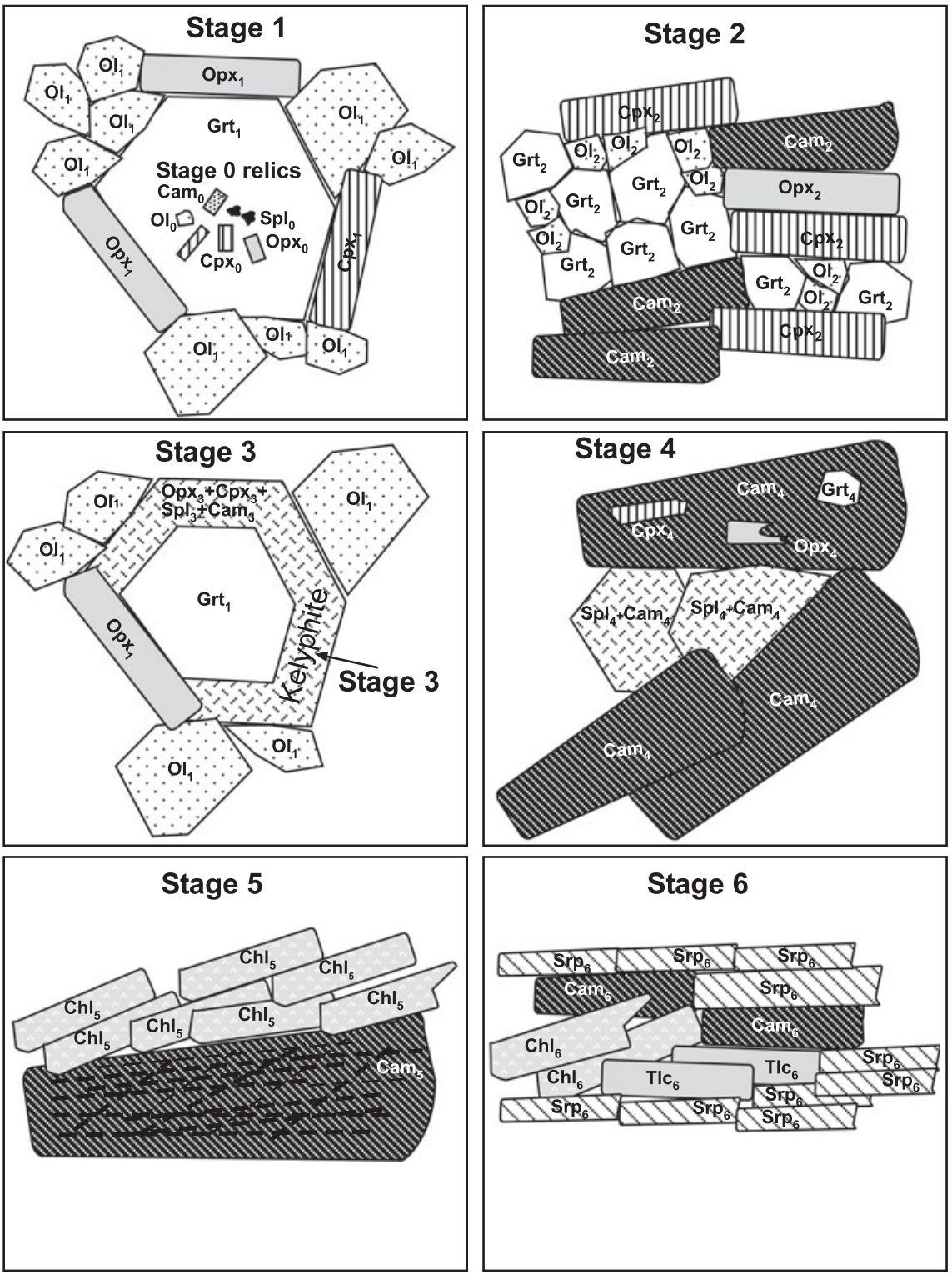



**Fig. 5.** Schematic line drawings showing the structural and mineralogical evolution in the garnet-bearing ultramafic rocks from stage 1 to stage 6.

Both reactions (Figs 5 & 6) are supported by microstructural and chemical evidence such as: (i) the disappearance of amphibole and spinel in the stage 1 assemblage and the mineral inclusions (representing relics of reactants) in $Grt_1$, (ii) the very low $Al_2O_3$ content in $Opx_1$, and (iii) the high pyrope content in

© 2007 Blackwell Publishing Ltd

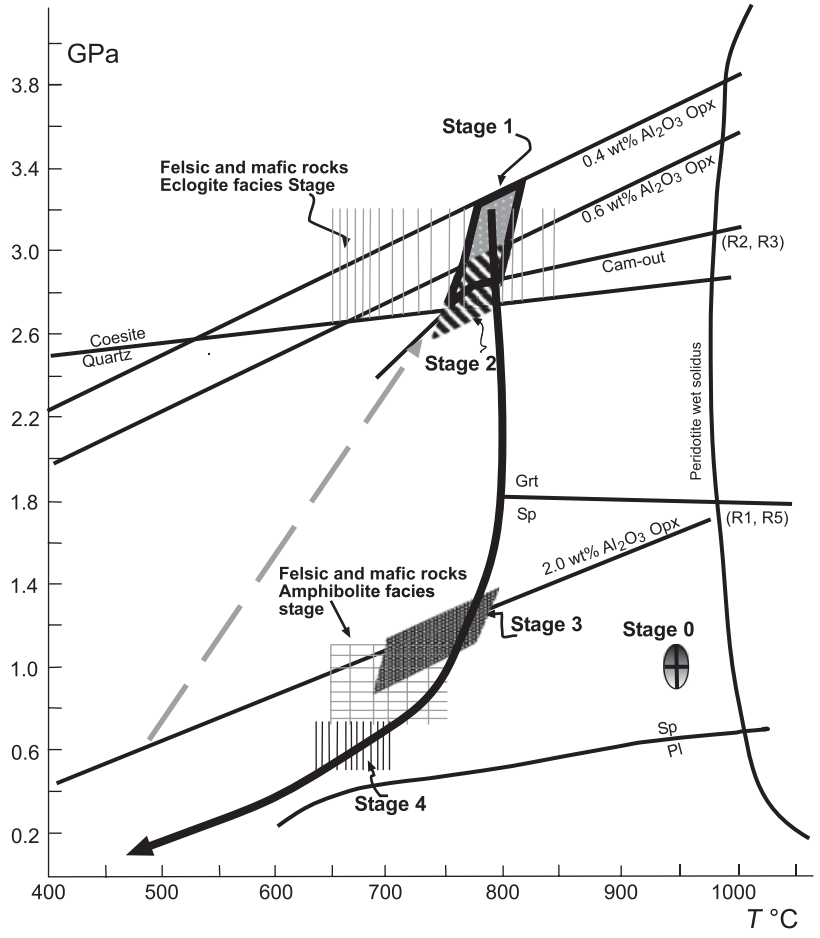



**Fig. 6.** Retrograde *P–T* path (thick black arrow) for the garnet-bearing ultramafic rocks. Mineral symbols according to Kretz (1983). Coesite-quartz curve after Bohlen & Boettcher (1982); Spl-lherzolite/Grt-lherzolite transition and Cam-out (NCFMASH system) from Fumagalli & Poli (2005); Pl-lherzolite-Spl-lherzolite transition (CMAS system) from Gasparik (1984); $Al_2O_3$ (wt%) isopleths from Wood (1974); peridotite wet solidus from Poli & Fumagalli (2003). *P–T* boxes are based on thermobarometric estimates. The *P–T* conditions of the protolith are reported along with the standard deviation. *P–T* boxes reconstructed for felsic and mafic rocks and including the prograde path (dashed arrow) for felsic rocks have been reported for comparison (Di Vincenzo *et al.*, 1997; Palmeri *et al.*, 2003).

$Grt_1$. The two reactions are promoted by increasing pressure (Poli & Fumagalli, 2003); moreover, the zoning in $Grt_1$ (in particular, the increase in the Fe/Mg ratio from core to inner rim) suggests that the increase in pressure from the spinel-bearing protolith (stage 0; Fig. 6) to UHP conditions (stage 1; Fig. 6) was accompanied by a decrease in temperature.

*Stage 2 – eclogite facies (fine-grained)*

The fine-grained stage 2 (Fig. 5; Table 3) is also an eclogite facies stage but can be distinguished from the previous stage mainly on the basis of the fine-grained texture (syntectonic recrystallization), the lack of kelyphite between garnet and olivine, and the presence of amphibole ($Cam_2$) as well as garnet, olivine, orthopyroxene and clinopyroxene. Moreover, the different garnet zoning between $Grt_2$ and $Grt_1$, the higher $Al_2O_3$ content in $Opx_2$ (comparable with that of $Opx_1$ rims), and the high $Al^{IV}$ content in $Cam_2$ suggest the recrystallization of garnet, olivine, clinopyroxene and orthopyroxene and a new crystallization of amphibole under decreasing pressure and increasing $a_{H_2O}$ conditions. Experimental reaction (R3), crossed in the inverse direction (Fig. 6), can be used to model the formation of amphibole (Niida & Green, 1999):

$$Cpx_1 + Grt_1 + Opx_1 + Ol_1 + H_2O = Cam_2. \quad (R3)$$

*Stage 3 – granulite facies to HP–HT amphibolite facies*

The assemblages observed in kelyphitic associations between $Grt_1$ and $Ol_1$ (i.e. $Opx_{3a}$ + $Cpx_3$ + $Spl_3$ in the inner portion near garnet and the mineral association $Opx_{3b} \pm Cam_3$ in the outer portion) represent a transitional granulite-amphibolite facies stage (Fig. 5). The two assemblages result from crossing $Grt_1$-$Ol_1$ breakdown reactions during decompression in the presence (R4 reaction) or absence (R5 reaction) of $H_2O$ (Obata & Thompson, 1981; Godard & Martin, 2000):

$$Grt_1 + Ol_1 + H_2O = Opx_{3b} + Spl_3 + Cam_3 \quad (R4)$$

$$Grt_1 + Ol_1 = Opx_{3a} + Cpx_3 + Spl_3. \quad (R5)$$

As observed by Godard & Martin (2000) for fixed *P–T* conditions and mineral compositions, reactions (R4) and (R5) are both equally possible; the presence

© 2007 Blackwell Publishing Ltd

of amphibole or pyroxene in kelyphite is thus determined by $P_{H_2O}$ fluctuations during exhumation.

*Stage 4 – HT–MP amphibolite facies*

This stage is characterized by the growth of large porphyroblastic $Cam_4$ ± green $Spl_4$ ± relic $Grt_4$ ± relic $Cpx_4$ and $Opx_4$ ± relic $Ol_4$ (Fig. 5). Amphibole has a lower $Al^{IV}$ content with respect to the granoblastic $Cam_2$ of eclogite stage 2. Clinopyroxene and garnet found within $Cam_4$ are minerals of eclogite stages 1 and 2, and are the reactants of the reaction (Zhang *et al.*, 1994):

$$Grt + Cpx + H_2O = Cam_4. \quad (R6)$$

The reaction is representative of amphibolite facies conditions and is responsible for the transformation of the garnet-bearing ultramafic rocks into amphibole-garnet fels.

*Stages 5 (low temperature–low pressure amphibolite facies) and 6 (greenschist facies)*

The assemblage Mg-Chl + tremolite (Tr) + serpentine (Serp) ± Tlc ± calcite (Cal) (Fig. 5) can be produced by the reaction (Sill, 1982):

$$Cam_4 + Opx + Ol + H_2O = Cam_5(Tr) + Chl + Na_2O. \quad (R7)$$

The progression of reaction (R7) transformed the stage 4 assemblage into a low-temperature amphibolite facies stage. The subsequent increase in water activity, together with a decrease in both temperature and pressure, led to the serpentinization of ultramafic rocks. The latter two stages are very rarely found in garnet-bearing pyroxenite, whereas they are diffuse in the metamorphic fels.

### *P–T* calculations

The equilibrium *P–T* conditions for each stage were estimated using various geothermobarometers. These include two independent barometers and seven thermometers: the Grt-Opx barometer (Al in Opx) with the calibrations of Harley (1984b) and Brey & Köhler (1990), and the Cpx-Grt Cr-exchange barometer (Nimis & Taylor, 2000); the Fe-Mg exchange thermometer between Grt-Opx (Harley, 1984a; Brey & Köhler, 1990), Grt-Cpx (Ellis & Green, 1979), Grt-Ol (O'Neill & Wood, 1979) and Grt-Hbl (Graham & Powell, 1984); the Cpx-Opx solvus (Taylor, 1998), the En-in Cpx (Nimis & Taylor, 2000) and Ca-in Opx (Brey & Köhler, 1990). Moreover, experimental data on pargasite stability in MORB pyrolite (Niida & Green, 1999) have been used to estimate *P–T* conditions of the protolith. Fe-Mg exchange thermometry is generally compromised by uncertainties in the $Fe^{3+}/Fe_{tot}$ ratio of both natural phases and the phases from which the thermometers were calibrated. However, as reported by Paquin & Altherr (2001), similar $Fe^{3+}$ contents have been found in garnet, Opx and Cpx, used to calibrate Fe-Mg exchange thermometers and natural samples. Apart from Cpx, published data on the $Fe^{3+}$ content in Grt and Opx from ultramafic rocks report low values (Zhang *et al.*, 1994; Krogh & Carswell, 1995); in this study, all Fe was considered to be ferrous. This assumption implies underestimation of temperature for Grt-Ol and Grt-Opx, whereas temperature is overestimated using the Grt-Cpx thermometer. The resulting *P–T* estimates are reported in Table 4.

*Stage 0 – spinel-bearing protolith*

The *P–T* conditions of the protolith can be defined through the Cr-exchange barometer, the Cpx-Opx solvus, the En-in Cpx and the composition of $Cam_0$ amphibole inclusions. Cpx thermobarometry yields an average temperature of 781 °C and pressure of 1.95 GPa, but lower average temperatures of 726 °C were obtained through Cpx-Opx solvus thermometry. On the contrary, higher temperatures and lower pressures (948 °C & 1 GPa) were obtained using the $Cam_0$ amphibole composition (Niida & Green, 1999). As results differ significantly, it is very difficult to interpret their meaning. One possibility is that inclusions within $Grt_1$ are relics of the reactants that generated garnet, and their present chemical composition may not represent the composition of the pristine phases of the protolith. Another possibility is that the very different estimates obtained using the various thermobarometric methods may represent different stages of equilibration during the transformation of the spinel-bearing protolith into the UHP garnet-bearing one. We prefer the latter hypothesis and believe that data obtained through $Cam_0$ compositions (948 °C; 1.0 GPa) best approximate the *P–T* conditions of the spinel-bearing protolith. The choice is based on observed compositional differences in $Cam_0$ (e.g. with the highest tschermakite component) with respect to the other analysed Cam in sample BC23, which indicate higher formation temperatures, and on the similarity in composition between some $Cpx_0$ and $Cpx_1$, which suggests a late re-equilibration of $Cpx_0$ with garnet.

*Stage 1*

The temperature for this stage was evaluated at the nominal pressure of 3.0 GPa based on phase equilibria constraints and using the core compositions of porphyroblastic minerals considered to preserve the metastable peak conditions. Although the different Fe-Mg exchange thermometers used to evaluate temperature have different blocking temperatures because of the differing diffusion rates of involved components, there is a good agreement of values between 764 and 837 °C (Table 4). Temperature estimates for

© 2007 Blackwell Publishing Ltd

**Table 4.** P–T estimates for samples BC23 (garnet-bearing ultramafic rock) and G12 (garnet-amphibole fels) samples.

| | Temperature ( °C) | | | | | | | | | | | | | | | | |
|---|---|---|---|---|---|---|---|---|---|---|---|---|---|---|---|---|---|
| | Cpx-Opx (Ta) (BK) | | | en-in Cpx (NT) | | Cam (NG) | | Grt-Opx (Ha) | | Grt-Cpx (EG) | | Ca-in Opx (BK) | | Grt-Ol (OW) | | Grt-Hbl (GP) | | |
| Sample | *n* | *T* | *T* | *n* | *T* | *n* | *T* | *n* | *T* | *n* | *T* | *n* | *T* | *n* | *T* | *n* | *T* | weghited average |
| BC23 | | | | | | | | | | | | | | | | | | |
| Stage 0 | 10 | 726 ± 49 | 704 ± 49 | 10 | 781 ± 67 | 11 | 948 ± 23 | | | | | | | | | | | |
| Stage 1 | 1 | 804 | 794 | 1 | 799 | | | 9 | 764 ± 13 | 1 | 820 | 8 | 792 ± 22 | 5 | 837 | | | 777 ± 45 |
| Stage 2 | 6 | 777 ± 34 | 759 ± 33 | 7 | 726 ± 29 | | | 1 | 749 | 8 | 775 ± 42 | 1 | 788 | 2 | 773 ± 1 | | | 755 ± 69 |
| Stage 3 | 6 | 759 ± 37 | 714 ± 34 | 4 | 760 ± 43 | | | 6 | 776 ± 30 | 6 | 705 ± 21 | | | | | | | 737 ± 77 |
| Stage 4 | | | | | | | | | | | | | | | | 1 | 629 | |
| G12 | | | | | | | | | | | | | | | | | | |
| Stage 4 | | | | | | | | | | | | | | | | 1 | 700 | |

| | Pressure (GPa) | | | | | | |
|---|---|---|---|---|---|---|---|
| | Cr-in Cpx (NT) | | Cam (NG) | | Al-in Opx (Hb) | | (BK) |
| | *n* | *P* | *n* | *P* | *n* | *P* | *P* |
| BC23 | | | | | | | |
| Stage 0 | 8 | 1.95 ± 0.7 | 11 | 1.0 ± 0.2 | | | |
| Stage 1 | 1 | 2.80 | | | 9 | 2.90 ± 0.18 | 3.67 ± 0.44 |
| Stage 2 | 7 | 3.2 ± 0.1 | | | 1 | 2.76 | 3.20 |
| Stage 3 | 4 | 0.8 ± 0.4 | | | 6 | 1.36 ± 0.4 | 0.92 ± 0.4 |

Reported estimates represent the average ± standard deviation ($2\sigma$) of values ($n > 1$) using different couples. For some stages the weighted average and error of temperature is also reported. Values for $n = 1$ refer to a single couple. n, number of couples used for calculation. Calibrations: Ta, Taylor (1998); NT, Nimis & Taylor (2000); NG, Niida & Green (1999); Ha and Hb, Harley (1984a,b; EG, Ellis & Green (1979); BK, Brey & Köhler (1990); OW, O'Neill & Wood (1979); GP, Graham & Powell (1984).

Grt-Opx, Grt-Ol and Ca-in-Opx thermometers are average values, whereas those estimated for Cpx-Opx, Grt-Cpx and En-in-Cpx are individual values. The lowest values were obtained using the Grt-Opx thermometer, whereas the highest refer to Grt-Ol estimates (Table 4). The Grt-Ol thermometer is characterized by large uncertainties and is strongly dependent on pressure (Taylor, 1998); if the olivine-garnet estimates are excluded, the calculated temperatures for the eclogite stage 1 are constrained to a narrower range (764–820 °C). Temperatures calculated with thermometers involving clinopyroxene are within the range reported above. The weighted average for Grt-Opx, Grt-Ol and Ca-in Opx estimates is 777 ± 45 °C.

Pressure values were calculated for a nominal temperature of 800 °C. Average pressure values are 2.90 GPa (Harley, 1984b calibration) and 3.67 GPa (Brey & Köhler, 1990 calibration); a value comparable with the Harley (1984b) estimate was obtained for Cr-in-Cpx applied to a single clinopyroxene. It is possible to compensate for the large difference between the two calibrations of the Al-in-Opx barometer by taking into consideration the isopleth for $Al_2O_3 = 0.4\%$ in $Opx_1$ (Fig. 6) corresponding to the lowest $Al_2O_3$ content in porphyroblastic $Opx_1$. The crossing of isopleth $Al_2O_3 = 0.4\%$ with the KD of temperatures constrains the maximum estimated pressures to between 3.2 and 3.3 GPa (Fig. 6). The estimated pressures for this stage agree with the lack of amphibole, the stability limit of which is around 3.0 GPa (Niida & Green, 1999).

*Stage 2*

Temperature and pressure estimates were calculated using the rim compositions of minerals in the fine-grained level because they are in equilibrium along their contact. Average estimates were calculated for Grt-Cpx, Cpx-Opx and En-in-Cpx thermometers at a nominal pressure of 3.0 GPa. Temperatures range from 726 to 788 °C, with the lowest value derived from the En-in-Cpx thermometer and the highest from the Ca-in-Opx thermometer. The weighted average temperature is 755 ± 69 °C. Pressure was mainly calculated with the Cr-in-Cpx barometer and yielded an average value of 3.2 GPa at a nominal temperature of 800 °C; the pressure estimated by the Al-in-Opx barometer yielded values of 2.76 and 3.2 GPa using the Harley (1984b) and Brey & Köhler (1990) calibrations, respectively. As for stage 1, the crossing of isopleth $Al_2O_3 = 0.6\%$ for $Opx_2$ with the KD of temperatures constrains the maximum estimated pressure to 3.0 GPa at 788 °C (Fig. 6). The presence in this stage of amphibole in equilibrium with the other phases (Table 3, Fig. 5) however, constrains pressures to below 2.9 GPa at 788 °C (Fig. 6). Comparing *P–T* estimates for the two eclogite stages and taking into account both the calculated weighted average and error for temperature, together with the mineral equilibrium and the reactions reported in the grid of Fig. 6, temperature equilibrium conditions recorded by the fine-grained layer are similar to those recorded by the medium-grained layer; however, the presence of amphibole and the higher $Al_2O_3$ contents in $Opx_2$ with

© 2007 Blackwell Publishing Ltd

respect to $Opx_1$ indicates that stage 2 mineral equilibrium was reached at slightly lower pressure conditions.

*Stage 3*

The Cpx and Opx in kelyphite and the rim of garnet in contact with kelyphite were used for temperature estimates. Resulting temperatures range between 705 and 776 °C, with the lowest temperature derived from the Grt-Cpx thermometer and the highest from the Grt-Opx thermometer. Comparable temperatures (714–760 °C) were obtained from the solvus Cpx-Opx and the En-in-Cpx. The weighted average temperature is 729 ± 77 °C. Pressures range widely from 0.8 to 1.36 GPa, with the lowest value for Cr-in-Cpx and the highest for Al-in-Opx. The very large standard deviations (see Table 4) for both barometers may partly be due to the very low Cr content in some Cpx grains, which influenced estimates based on Cr-in-Cpx. However, the crossing of the 2 wt% $Al_2O_3$ isopleth for orthopyroxene (representing the $Al_2O_3$ content close to $Opx_3$) with the calculated KD of temperature constrains pressures to nearly 1.1–1.3 GPa.

*Stage 4*

The Grt-Hbl thermometer applied to the rim of garnet enclosed in porphyroblastic amphibole yielded temperatures of 629–700 °C and defines the range of temperatures during the HT amphibolite stage. Pressure is unconstrained for this stage.

*Stage 5 and 6*

The tremolite-chlorite association is stable at 600 °C and ~0.5 GPa (Sill, 1982): these *P–T* conditions can be ascribed to the low-temperature amphibolite facies (stage 5). Finally, the stage 6 assemblage is indicative of greenschist facies conditions, possibly at 350–400 °C (Spear, 1993) and pressures below 0.5 GPa, and may reflect late-stage cooling and/or unloading.

### *P–T* path

Data on the different assemblages and thermobarometric estimates for the garnet-bearing ultramafic rocks describe an evolution which began with the formation of the protolith, followed by a UHP metamorphic history, to near-complete exhumation. The *P–T* box describing the physical conditions for eclogite stage 1 is constrained towards lower pressures by the amphibole stability curve (Fumagalli & Poli, 2005) and towards higher pressures by the $Al_2O_3$ isopleth in orthopyroxene (Fig. 6). Note that the *P–T* stage 1 is within the coesite stability field, although no coesite was found in these ultramafic rocks. After the attainment of peak conditions, decompression occurred under nearly isothermal conditions during eclogite stage 2. The *P–T* box (Fig. 6) for this stage is intersected by the stability curve of amphibole and by that of the quartz-coesite transition. The presence of amphibole suggests that the observed assemblage mainly formed below the Cam-out curve (Fig. 6).

The development of kelyphite (granulite/HP amphibolite facies stage 3) is evidence for a drop in pressure under nearly isothermal conditions. The *P–T* box (Fig. 6) for this stage is constrained by thermobarometric estimates and by the aluminium content of orthopyroxene. The last portion of the retrogressive *P–T* path, a typical cooling–unloading path, is mainly constrained by the calculated temperature range for the HT, MP amphibolite facies stage and by the mineral assemblages of the two amphibolite stages (4 and 5) and greenschist facies stage 6.

The retrograde *P–T* path is characterized by a nearly isothermal decompression path from eclogite facies, corresponding to mantle depth, to granulite/HP amphibolite facies conditions, which were achieved at deep crustal levels (~30–40 km), and by a final decrease in both pressure and temperature from deep/intermediate to shallow crustal levels. The obtained *P–T* values for felsic and mafic rocks (Palmeri *et al.*, 2003) of the Lanterman Range and those reconstructed in this paper for garnet-bearing ultramafic rocks are compared in Fig. 6. The figure shows that the metamorphic peak conditions estimated for felsic, mafic and ultramafic rocks overlap. In particular, the garnet-bearing ultramafic rocks better constrain the maximum pressure for UHP conditions, and for the first time provide evidence of very early-stage exhumation under eclogite facies conditions (stage 2). Moreover, there is a clear continuity among the different *P–T* boxes reconstructed for stage 3 (granulite-HP/HT amphibolite facies stage) in the ultramafic rocks, the MP amphibolite facies for felsic and mafic rocks, the HT–MP amphibolite facies in the ultramafic rocks, and the LP amphibolite facies in mafic rocks. This implies that the reconstructed retrograde *P–T* path for the garnet-bearing ultramafic rocks overlaps with that reconstructed for felsic and mafic rocks (Palmeri *et al.*, 2003) and supports the idea that mafic, ultramafic and felsic rocks in the Lanterman Range were associated before UHP conditions and were contemporaneously exhumed as an unit. The type of retrograde *P–T* path suggests a two-stage process of exhumation: initial isothermal decompression from mantle depths to deep crustal levels, followed by cooling-unloading from deep–intermediate to upper crustal levels. As for the rate of exhumation, the overlapping of Sm-Nd, U-Pb and Ar-Ar ages in minerals with different closure temperatures was considered as evidence for rapid cooling (Di Vincenzo *et al.*, 1997, 2001). In particular, Di Vincenzo & Palmeri (2001) estimated an exhumation rate of 3–4 mm $a^{-1}$ for mafic eclogites between 1.6 and 0.5 GPa. This, however, is a minimum estimate and it was probably higher at the start of exhumation between ~3 and 1.6 GPa.

© 2007 Blackwell Publishing Ltd

## MECHANICS OF EXHUMATION

Evidence from felsic, mafic and ultramafic rocks in the Lanterman Range, as: (i) the common pervasive metamorphic foliation developed under amphibolite facies conditions and the younger deformation phases developed under lower-grade conditions (Capponi *et al.*, 1997), and (ii) the comparable metamorphic evolution from UHP conditions to greenschist facies, indicate that these rocks underwent exhumation as a single tectonic melange. It is shown here that the densities and rheological properties of these rocks are compatible with this scenario.

Exhumation velocities in the steep portion of retrograde *P–T* paths are often of the same order as subduction velocities (Rubatto & Hermann, 2001). The fast exhumation of subducted continental material (including the incorporated mafic and ultramafic components) is usually attributed to the upward buoyancy of the material because of its lower density with respect to the surrounding mantle (Cloos & Shreve, 1988; Chemenda *et al.*, 1995, 1996; Ernst *et al.*, 1995, 1997). The process can be modelled in terms of shear resistance along the shear zones decoupling the exhuming slices from the surrounding material (Chemenda *et al.*, 1995, 1996; Ernst *et al.*, 1995, 1997; Ernst, 2001; Ranalli, 2003; Ranalli *et al.*, 2005) or, in terms of the bulk rheology (effective viscosity) of the exhuming UHP rocks in the subduction channel (Mancktelow, 1995; Burov *et al.*, 2001; Gerya *et al.*, 2002; Jolivet *et al.*, 2005).

Assuming that exhumation occurs when the upward buoyancy of the material overcomes the resistance to detachment along two shear zones (a reverse-sense shear zone at the base of the exhuming slice, and a normal-sense shear zone at the top; Duchêne *et al.*, 1997; Ernst, 2001; Lardeaux *et al.*, 2001), the condition for exhumation can be written approximately as (Ranalli, 2003; Ranalli *et al.*, 2005; only absolute values are considered)

$$\Delta\rho_c g D L \sin\delta > 2\tau L \qquad \text{(R8)}$$

where $\Delta\rho_c$ is the density difference between the exhuming material and the surrounding mantle, $g$ is the acceleration of gravity, $D$ and $L$ respectively the thickness and downdip length of the exhuming slice, $\delta$ the subduction dip angle, and $\tau$ the resistance to shear detachment along shear zones. The left-hand side of equation (R8) represents the component in the up-dip direction (parallel to the subduction channel) of the upward buoyancy of the slice; the right-hand side of the equation represents the total resistance to detachment, which is assumed to act in two shear zones at the top and bottom of the slice.

In terms of the critical density difference, the condition for exhumation is therefore

$$\Delta\rho_c > \beta(\tau/gD) \qquad \text{(R9)}$$

where $\beta$ is a dimensionless factor ranging from 2 to 5 for vertical (90°) to shallow (25°) subduction angles. Both $\Delta\rho_c$ and $\tau$ are functions of composition, degree of metamorphism and temperature (depth). Greater slice thickness reduces the required density difference, as the anomalous volume increases.

In the present case, it is estimated that volume fractions in the exhumed material are: 0.80 felsic host gneiss, 0.15 mafic eclogite and 0.05 ultramafic rocks. *In situ* densities are difficult to estimate because of the uncertain amount of retrogression. According to Bousquet *et al.* (1997) and Ernst *et al.* (1997), the densities of the three components of the exhumed material are in the ranges of 3.08–3.18, 3.56–3.83 and 3.37–3.38 $\times 10^3$ kg m$^{-3}$, respectively (the latter value may also be considered the density of the surrounding mantle; Anderson, 1989). Considering average values for the density components, $\Delta\rho_c$ for the exhumed material in the Lanterman Range that was subducted to subcrustal depths is $\sim$150 kg m$^{-3}$.

Estimates of shear strength in the ductile field strongly depend on grain size, which determines whether nonlinear (power-law) or linear (diffusion) creep is the predominant deformation mechanism. At upper mantle temperatures, power-law creep strengths at geological strain rates are usually low, i.e. $\tau \leq 0.1$–10 MPa (Ranalli, 1995). A 1 order of magnitude increase in strain rate (to be expected if deformation is concentrated in shear bands) increases the strength by a factor of $\sim$2. Under a differential stress of $\sim$10 MPa, strain rates for the relevant materials are in the $10^{-8}$–$10^{-12}$ s$^{-1}$ range, with felsic rocks being the weakest, followed in order of increasing strength by intermediate, mafic and ultramafic rocks; garnet-rich rocks are the strongest (Wilks & Carter, 1990; Ranalli, 1995; Jin *et al.*, 2001). At small grain sizes (≤10–100 $\mu$m, depending on the material) diffusion creep becomes predominant, with a consequent drop in strength (Wang & Ji, 2000; Dimanov & Dresen, 2005). If experimental conditions are extrapolated to the strain rates ($\sim 10^{-11}$–$10^{-13}$ s$^{-1}$) in narrow shear zones ($\sim$10–1000 m thick) whose sides move at velocities on the order of 1 cm a$^{-1}$, resulting creep strengths are 1 MPa or less in power-law creep and lower in diffusion creep. All things considered, it seems reasonable to set $\tau = 1$ MPa in equation (R9); consequently, the exhumation of slices a few kilometres thick by buoyancy contrast is indeed possible, as observed in the Lanterman Range.

The same conclusion is reached by modelling the process in terms of the bulk rheology of the exhumed material. Raimbourg (2005) proposed the use of the exhumation number $\alpha$, which describes the capacity of a material to be exhumed. It is defined as

$$\alpha = \frac{\partial\varphi}{\partial x}\frac{h^2}{\eta v} \qquad \text{(R10)}$$

where $\partial\varphi/\partial x$ is the hydraulic potential gradient along the subduction channel (downward direction $x$), $h$ an

© 2007 Blackwell Publishing Ltd

arbitrary normalizing width, $\eta$ the viscosity of the subducted material, and $v$ the subduction velocity. Exhumation is possible for a wide range of densities (which affect the hydraulic potential) and viscosities.

This approach is not directly applicable to the rocks in the Lanterman Range because of the lack of detailed structural data, but estimated viscosities and densities appear to be of the right order of magnitude. The above considerations provide only a rough description of the process, but are sufficient to demonstrate that rapid exhumation of material in the Lanterman Range, as petrological and geochronological (Di Vincenzo & Palmeri, 2001) data indicate, is compatible with the mechanical properties of the subducted material.

## DISCUSSION

Based on the *P–T–t* evolution reconstructed for felsic and mafic rocks and on the geochemistry of mafic rocks, Palmeri *et al.* (2003) proposed an arc-continent collision setting for the Lanterman Range. The pre-orogenic setting of mafic and felsic rocks along the eastern Wilson Terrane, including the protoliths of the HP and UHP rocks, could be restored to a back-arc position in the over-riding plate with respect to the Bowers Terrane volcanic arc (Palmeri *et al.*, 2003). In this setting, felsic rocks derive from a typical continental siliciclastic sediment which is interlayered with mafic rocks, whose geochemical affinity includes E-MORB, T-MORB and orogenic calcalkaline types (Di Vincenzo *et al.*, 1997).The variabiliy of geochemical features of mafic rocks of Lanterman Range is also documented in the mafic rocks of Bowers Terrane (Rocchi *et al.*, 2003). Felsic and mafic rocks were subsequently involved in a subduction–collision system and coupled with the subducting slab because of oceanward migration of arc magmatism and tectonism, possibly related to slab rollback. In this scenario, several issues must be addressed to understand the significance and role of ultramafic rocks and to reconstruct the context of the evolution of the palaeo-Pacific margin of Gondwana (Kleinschmidt & Tessensohn, 1987; Ricci *et al.*, 1997), namely the nature and origin of the ultramafic igneous protoliths, their *P–T–t* evolution, and how and when they came to be juxtaposed with the felsic and mafic rocks.

As for the nature and origin of these protoliths, the chemical composition of the garnet-bearing ultramafic rocks is similar to that of the olivine-poor garnet lherzolite (PX composition) used by Fumagalli & Poli (2005) in experiments on hydrous mantle peridotites. The mineral assemblage of the protolith (now found as inclusions within garnet) can be referred either to an igneous ultramafic rock or to an ultramafic granulite. Although with some uncertainty, *P–T* estimates indicate that the protolith formed within the spinel-bearing lherzolite field. Furthermore, some mineral features such as: (i) the high $Al_2O_3$ content in $Opx_0$, (ii) the high forsterite content in $Ol_0$, and (iii) the high $Cr_2O_3$ in dark $Spl_0$ and its $Fe^{2+}/Fe^{2+} + Mg$ and $Cr/Cr + Al$ ratios suggest that the spinel-bearing ultramafic protoliths likely belong to an upper mantle association rather than to a crustal layered complex (Haggerty, 1990).

As for the *P–T–t* evolution, the previous discussion demonstrates that the retrograde path is well-constrained for the UHP felsic, mafic and ultramafic rocks of the Lanterman Range. However, the prograde path of felsic/mafic rocks (Fig. 6) likely differed from that of ultramafic ones. Petrological evidence shows that felsic and mafic rocks followed a clockwise prograde path before UHP metamorphism, whereas the path of ultramafic rocks is difficult to reconstruct. The only available data on physical conditions are the HT and LP values obtained for the relic minerals of stage 0 and the UHP conditions estimated for stage 1. The two data points only indicate that a loading coupled with a cooling process occurred between these two stages.

Previous conclusion that ultramafic rocks belong to an upper mantle association rather than to a crustal layered intrusive complex suggests that juxtaposition with the felsic and mafic material occurred during subduction. In this framework, the protoliths of the garnet-bearing ultramafic rocks from the Lanterman Range can be seen as spinel-bearing ultramafic rocks belonging to a 'mantle peridotite' association (Brueckner & Medaris, 2000), which originated in the mantle wedge above the subduction zone between the palaeo-Pacific plate and the Gondwana continental margin. In the above geological context, the ultramafic rocks were probably incorporated into the subduction channel as tectonic slices or sinking blobs (Brueckner, 1998) within felsic and mafic rocks, possibly because of convective flow within the wedge induced by the downgoing slab (Iwamori, 1997).

After incorporation into the subducting plate, the ultramafic rocks, together with the felsic and mafic rocks, underwent UHP metamorphism and subsequent exhumation. Modelling of the exhumation process demonstrates that the mechanical properties of the subducted material are compatible with syn-subduction exhumation of the Lanterman rocks (in slices a few kilometres thick) during continued lithospheric convergence. The two-stage exhumation path inferred from petrological and geochronological data is common to other UHP belts, such as those of the Variscan and Alpine orogens (Spalla *et al.*, 1996; Duchêne *et al.*, 1997; Ranalli *et al.*, 2005). The first stage, represented by fast isothermal unloading and characterizing the start of exhumation to deep crustal levels, is attributed to buoyancy-driven extrusion (Chemenda *et al.*, 1995, 1996; Ernst *et al.*, 1997; Ranalli *et al.*, 2005); the second stage, characterized by a contemporaneous cooling and unloading to shallow crustal levels, may be linked to slab break-off and consequent lithospheric rebound and crustal extension.

© 2007 Blackwell Publishing Ltd

## CONCLUSIONS

**1** Garnet-bearing ultramafic rocks are minor but important components of the HP–UHP belt of the Lanterman Range. They record UHP peak metamorphic conditions of 3.2–3.3 GPa and 764–820 °C and a multistage retrograde evolution up to greenschist facies with pressure below 0.5 GPa and temperature between 300 and 400 °C. The retrograde *P–T* path is nearly isothermal from UHP conditions up to deep crustal levels, and becomes a cooling–unloading path from intermediate to shallow levels.

**2** The chemical composition of the garnet-bearing ultramafic rocks together with the mineral assemblage of the protolith (now found as inclusions within garnet) suggests an igneous ultramafic rock formed within the spinel-bearing lherzolite stability field. Subduction of these protoliths resulted in the development of garnet-bearing assemblages at UHP conditions of metamorphism.

**3** The context of UHP metamorphism in the Lanterman Range (northern Victoria Land, Antarctica) is the subduction of the palaeo-Pacific plate under the Gondwana continental margin. In this scenario, HP–UHP belt of the Lanterman Range originated from an arc-continent collision setting. The pre-orogenic mafic and felsic rocks, including the protoliths of the HP and UHP rocks, could be restored to a back-arc position in the over-riding plate and ultramafic rocks probably originated in the mantle wedge above the subduction zone. Felsic, mafic and ultramafic rocks were involved in a subduction–collision system and coupled with the subducting slab. After incorporation into the subducting plate the ultramafic rocks, together with the felsic and mafic rocks, underwent UHP metamorphism and subsequent exhumation.

**4** Modelling of the exhumation process demonstrates that the mechanical properties of the subducted material are compatible with a syn-subduction exhumation.

## ACKNOWLEDGEMENTS

This research was carried out with the financial support of MIUR-PRIN 2003 (C.A. Ricci) and Siena University-PAR 2003 (R. Palmeri). G. Ranalli's research is also supported by a grant from NSERC (Natural Sciences and Engineering Research Council of Canada).The Italian 'Programma Nazionale di Ricerche in Antartide' is thanked for the invaluable support in the field during the 1996–97 ItaliAntartide expedition. We are grateful to thorough reviews by S. Elvevold and an anonymous together with J. Gilotti for editorial handling. The authors fondly remember F. Olmi who kindly assisted during microprobe work and would like to dedicate this paper to the memory of V. Trommsdorff, one of the investigators of MIUR-PRIN 2003 research group, for stimulating discussions, fruitful ideas and precious advice on the petrology of garnet-bearing ultramafic rocks.

## REFERENCES

Anderson, D. L., 1989. *Theory of the Earth*. Blackwell, Oxford.

Bohlen, S. R. & Boettcher, A. L., 1982. The quartz-coesite transformation: a pressure determination and the effects of other composition. *Journal of Geophysical Research*, **87,** 7073–7078.

Borg, S. G. & De Paolo, D. J., 1994. Laurentia, Australia and Antarctica as a Late Proterozoic supercontinent: constraints from isotopic mapping. *Geology*, **22,** 307–310.

Bousquet, R., Goffé, B., Henry, P., Le Pichon, X. & Chopin, C., 1997. Kinematic, thermal and petrological model of the central Alps: Lepontine metamorphism in the upper crust and eclogitisation of the lower crust. *Tectonophysics*, **273,** 105–127.

Bradshaw, J. D. & Laird, M. G., 1983. The pre-Beacon geology of northern Victoria Land: a review. In: *Antarctic Earth Science* (eds Oliver, R. H., James, P. R. & Jago, J. B.), pp. 98–101. Australian Academy of Sciences, Canberra.

Brey, G. P. & Köhler, T., 1990. Geothermobarometry in four-phase lherzolites II. New thermobarometers, and practical assessment of existing thermobarometers. *Journal of Petrology*, **31,** 1353–1378.

Brueckner, H. K., 1998. Sinking intrusion model for the emplacement of garnet-bearing peridotites into continent collision orogens. *Geology*, **26,** 631–634.

Brueckner, H. K. & Medaris, L. G., 1998. A tale of two orogens-the contrasting P–T–t history and geochemical evolution of mantle in ultrahigh pressure (UHP) metamorphic terranes of the Norwegian Caledonides and the Czech Variscides. *Schweizerische Mineralogische und Petrographische Mitteilungen*, **78,** 293–307.

Brueckner, H. K. & Medaris, L. G., 2000. A general model for the intrusion and evolution of "mantle" garnet peridotites in high-pressure and ultra-high-pressure metamorphic terranes. *Journal of Metamorphic Geology*, **18,** 123–133.

Burov, E., Jolivet, L., Le Pourhiet, L. & Poliakov, A., 2001. A thermomechanical model of exhumation of high pressure (HP) and ultra-high pressure (UHP) metamorphic rocks in Alpine-type collision belts. *Tectonophysics*, **342,** 113–136.

Capponi, G., Castelli, D., Fioretti, A. M. & Oggiano, G., 1997. Geological mapping and field relationships of eclogites from the Lanterman Range (northern Victoria Land, Antarctica). In: *The Antarctic region: geological evolution and processes* (ed. Ricci, C. A.), pp. 219–226. Terra Antartica Publications, Siena.

Carswell, D. A., Harvey, M. A. & Al-Samman, A., 1983. The petrogenesis of contrasting Fe-Ti and Mg-Cr garnet peridotite types in the high grade gneiss complex of Western Norway. *Bulletin Minéralogie*, **106,** 727–750.

Chemenda, A. I., Mattauer, M., Malavieille, J. & Bokun, A. N., 1995. A mechanism for syn-collisional rock exhumation and associated normal faulting: results from physical modelling. *Earth and Planetary Science Letters*, **132,** 225–232.

Chemenda, A. I., Mattauer, M. & Bokun, A. N., 1996. Continental subduction and a mechanism for the exhumation of high-pressure metamorphic rocks: new modelling and field data from Oman. *Earth and Planetary Science Letters*, **143,** 173–182.

Cloos, M. & Shreve, R. L., 1988. Subduction-channel model of prism accretion, mélange formation, sediment subduction, and subduction erosion at convergent plate margins. *Pure Applied Geophysics*, **128,** 455–499.

Coleman, R. G., Beatty, L. B. & Brannock, W. W., 1965. Eclogites and eclogites: their differences and similarities. *Geological Society of America Bulletin*, **76,** 483–508.

Di Vincenzo, G. & Palmeri, R., 2001. An $^{40}$Ar-$^{39}$Ar investigation of high-pressure metamorphism and the retrogressive history of mafic eclogites from the Lanterman Range (Antarctica):

© 2007 Blackwell Publishing Ltd

evidence against a simple temperature control on argon transport in amphibole. *Contributions to Mineralogy and Petrology*, **141,** 15–35.

Di Vincenzo, G., Palmeri, R., Talarico, F., Andriessen, P. A. & Ricci, C. A., 1997. Petrology and geochronology of eclogites from the Lanterman Range, Antarctica. *Journal of Petrology*, **38,** 1391–1417.

Di Vincenzo, G., Ghiribelli, B., Giorgetti, G. & Palmeri, R., 2001. Evidence of a close link between petrology and isotope records: constraints from SEM, EMP, TEM and in situ $^{40}Ar$-$^{39}Ar$ laser analyses on multiple generations of white micas (Lanterman Range, Antarctica). *Earth and Planetary Science Letters*, **192/3,** 389–405.

Dimanov, A. & Dresen, G., 2005. Rheology of synthetic anorthite-diopside aggregates: implications for ductile shear zone. *Journal of Geophysical Research*, **110,** doi: B07203, 10.1029/2004JB003431.

Duchêne, S., Lardeaux, J. M. & Albarède, F., 1997. Exhumation of eclogites: insights from depth-time path analysis. *Tectonophysics*, **280,** 125–140.

Ellis, D. S. & Green, D. H., 1979. An experimental study on the effect of Ca upon garnet-clinopyroxene Fe-Mg exchange equilibria. *Contributions to Mineralogy and Petrology*, **71,** 13–22.

Ernst, W. G., 2001. Subduction, ultra-high pressure metamorphism, and regurgitation of buoyant crustal slices – implications for arcs and continental growth. *Physics Earth Planetary International*, **127,** 253–275.

Ernst, W. G., Liou, J. G. & Coleman, R. G., 1995. Comparative petrotectonic study of five Eurasian ultrahigh-pressure metamorphic complexes. *International Geologic Review*, **37,** 191–211.

Ernst, W. G., Maruyama, S. & Wallis, S. R., 1997. Buoyancy-driven, rapid exhumation of ultrahigh-pressure metamorphosed continental crust. *Proceedings of the National Academy of Sciences of the United States of America*, **94,** 9532–9537.

Evans, B. W. & Trommsdorff, V., 1978. Petrogenesis of garnet-lherzolite, Cima di Gagnone, Lepontine Alps. *Earth and Planetary Science Letters*, **40,** 333–348.

Fumagalli, P. & Poli, S., 2005. Experimentally determined phase relations in hydrous peridotites to 6.5 GPa and their consequences on the dynamics of subduction zones. *Journal of Petrology*, **46,** 555–578.

Gasparik, T., 1984. Experimental determined stability of clinopyroxene + garnet + corundum in the system CaO-MgO-$Al_2O_3$-$SiO_2$. *American Mineralogist*, **69,** 1025–1035.

Gerya, T. V., Stockhert, B. & Perchuk, A. L., 2002. Exhumation of high-pressure metamorphic rocks in a subduction channel: a numerical simulation. *Tectonics*, **21,** 1056.

Ghiribelli, B., Frezzotti, M. L. & Palmeri, R., 2002. Coesite in eclogites of the Lanterman Range (Antarctica): evidence from textural and raman spectroscopy studies. *European Journal of Mineralogy*, **14,** 355–360.

Godard, G. & Martin, S., 2000. Petrogenesis of kelyphites in garnet peridotites: a case study from the Ulten zone, Italian Alps. *Journal of Geodynamics*, **30,** 117–145.

Graham, C. M. & Powell, R., 1984. A garnet-hornblende geothermometer: calibration testing and application to the Pelona schist, southern California. *Journal of Metamorphic Geology*, **2,** 13–31.

Grew, E. S. & Sandiford, M., 1984. A Staurolite-talc assemblage in tourmaline-phlogopite-chlorite schist from northern Victoria Land, Antarctica, and its petrogenetic significance. *Contributions to Mineralogy and Petrology*, **87,** 337–350.

Grew, E. S., Kleinschmidt, G. & Schubert, W., 1984. Contrasting metamorphic belts in North Victoria Land, Antarctica. In: *German Antarctic North Victoria Land Expedition 1982/83*, GANOVEX III (ed. Roland, N. W.), *Geologische Jahrbuch*, **0B60,** 253–263.

Haggerty, S. E., 1990. Oxide mineralogy of the upper mantle. In: *Modern Methods of Igneous Petrology – Understanding Magmatic Processes* (eds Nicholls, J. & Russell, J. K.). *Reviews in Mineralogy*, **24,** 355–372.

Harley, S. L., 1984a. An experimental study of the partitioning of Fe and Mg between garnet and orthopyroxene. *Contributions to Mineralogy and Petrology*, **86,** 359–373.

Harley, S. L., 1984b. The solubility of alumina in orthopyroxene coexisting with garnet in FeO-MgO-$Al_2O_3$-$SiO_2$ and CaO-FeO-MgO-$Al_2O_3$-$SiO_2$. *Journal of Petrology*, **25,** 665–696.

Holland, T. J. B. & Blundy, J. D., 1994. Non-ideal interactions in calcic amphiboles and their bearing on amphibole-plagioclase thermometry. *Contributions to Mineralogy and Petrology*, **116,** 433–447

Iwamori, H., 1997. Compression melting in subduction zones. *Terra Nova*, **9,** 9–13.

Jackson, J. A., 1997. *Glossary of Geology*. American Geological Institute, Alexandria, VA, pp. 769.

Jin, Z. M., Zhang, S., Green, H. V. & Jin, S., 2001. Eclogite rheology: implications for subducted lithosphere. *Geology*, **29,** 667–670.

Jolivet, L., Raimbourg, H., Labrousse, L., Avigad, D., Leroy, Y., Austrheim, H. & Andersen, T. B., 2005. Softening triggered by eclogitization, the first step toward exhumation during continental subduction. *Earth and Planetary Science Letters*, **237,** 532–547.

Kalt, A., Altherr, R. & Hanel, M., 1995. Contrasting P–T conditions recorded in ultramafic high pressure rocks from the Variscan Schwarzwald (F.R.G.). *Contributions to Mineralogy and Petrology*, **121,** 45–60.

Kleinschmidt, G. & Tessensohn, F., 1987. Early Paleozoic westward subduction at the Pacific margin of Antarctica. In: *Gondwana Six: Structure, Tectonics and Geophysics; Geophysical Monograph 40,* (ed. McKenzie, G. D.), pp. 89–105. American Geophysical Union, Washington, DC.

Kleinschmidt, G., Schubert, W., Olesch, M. & Rettmann, E., 1987. Ultramafic rocks of the Lanterman Range in north Victoria Land, Antarctica: petrology, geochemistry and geodynamic implications. *Geologisches Jahrbuch B*, **66,** 231–273.

Kretz, R., 1983. Symbols for rock-forming minerals. *American Mineralogist*, **68,** 277–279.

Krogh, E. J. & Carswell, D. A., 1995. HP and ultrahigh-P eclogites and garnet peridotites in the Scandinavian Caledonides. In: *Ultrahigh Pressure Metamorphism* (eds Coleman, R. G. & Wang, X.), pp. 244–298. Cambridge University Press, Cambridge.

Lardeaux, J. M., Ledru, P., Daniel, I. & Duchêne, S., 2001. The Variscan French Massif Central – a new addition to the ultrahigh pressure metamorphic club: exhumation process and geodynamic consequences. *Tectonophysics*, **332,** 143–167.

Le Maitre, R. W., 1976. Some problems of the projection of chemical data into mineralogical classification. *Contributions to Mineralogy and Petrology*, **56,** 181–189.

Leake, B. E., Wooley, A. R. & Arps, C. E. S., 1997. Nomenclature of amphiboles. Report of the subcommittee on amphiboles of the International mineralogical association commission on new minerals and mineral names. *European Journal of Mineralogy*, **9,** 623–651.

Liou, J. G. & Carswell, D. A., 2000. Garnet peridotites and ultrahigh.pressure minerals. Preface. *Journal of Metamorphic Geology*, **18,** 121.

Mancktelow, N. S., 1995. Non-lithostatic pressure during sediment subduction and the development of exhumation of high pressure metamorphic rocks. *Journal of Geophysical Research*, **100,** 571–583.

Niida, K. & Green, D. H., 1999. Stability and chemical composition of pargasitic amphibole in MORB pyrolite under upper mantle conditions. *Contributions to Mineralogy and Petrology*, **135,** 18–40.

Nimis, P. & Taylor, W. R., 2000. Single clinopyroxene thermobarometry for garnet peridotites. Part I. Calibration and testing of a Cr-in Cpx barometer and an enstatite-in Cpx thermometer. *Contributions to Mineralogy and Petrology*, **139,** 541–544.

O'Neill, H. St C. & Wood, B. J., 1979. An experimental study of Fe-Mg partitioning between garnet and olivine and its cali-

© 2007 Blackwell Publishing Ltd

bration as a geothermometer. *Contributions to Mineralogy and Petrology*, **70,** 59–70.
Obata, M. & Thompson, A. B., 1981. Amphibole and chlorite in mafic and ultramafic rocks in the lower crust and upper mantle. *Contributions to Mineralogy and Petrology*, **77,** 74–81.
Palmeri, R., Ghiribelli, B., Talarico, F. & Ricci, C. A., 2003. Ultra-high-pressure metamorphism in felsic rocks: the garnet-phengite gneisses and quartzites from the Lanterman Range, Antarctica. *European Journal of Mineralogy*, **15,** 513–525.
Paquin, J. & Altherr, R., 2001. New constraints on the P–T evolution of the Alpi Arami garnet peridotite body (central Alps, Switzerland). *Journal of Petrology*, **42,** 1119–1140.
Pearson, D. G., Davies, G. R. & Nixon, P. H., 1995. Orogenic ultramafic rocks of UHP (diamond facies) origin. In: *Ultra-high Pressure Metamorphism* (eds Coleman, R. G. & Wang, X.), pp. 456–511. Cambridge University Press, Cambridge.
Poli, S. & Fumagalli, P., 2003. Mineral assemblages in ultrahigh pressure metamorphism: a review of experimentally determined phase diagrams. In: *Ultrahigh Pressure Metamorphism* (eds. Carswell, D. A. & Compagnoni, R.), pp. 307–340. EMU n. 5, Eötvös University Press, Budapest.
Raimbourg, H., 2005. Mécanismes d'éclogitisation et consequences pour l'exhumation des roches métamorphiques de haute pression. Ph. D. thesis, Univ. Paris VI, 407 pp.
Ranalli, G., 1995. *Rheology of the Earth*, 2nd edn. Chapman & Hall, London.
Ranalli, G., 2003. A model of Palaeozoic subduction and exhumation of continental crust: the Ulten Unit, Tonale Nappe, eastern Austroalpine. *Memorie Società Geologica, Univ. Padova*, **54,** 205–208.
Ranalli, G., Martin, S. & Mahatsente, R., 2005. Continental subduction and exhumation: an example from the Ulten Unit, Tonale Nappe, eastern Austroalpine. *Geological Society London, Special Publication*, **243,** 159–174.
Ricci, C. A., Talarico, F., Palmeri, R., Di Vincenzo, G. & Pertusati, P. C., 1996. Eclogite at the Antarctic Paleo-Pacific active margin of Gondwana (Lanterman Range, northern Victoria Land, Antarctica). *Antarctic Sciences*, **8,** 277–280.
Ricci, C. A., Talarico, F. & Palmeri, R., 1997. Tectonothermal evolution of the Antarctic paleo-pacific active margin of Gondwana: a northern Victoria Land perspective. In: *The Antarctic Region: Geological Evolution and Processes* (ed. Ricci, C. A.), pp. 213–218. Terra Antartica Publications, Siena.
Rocchi, S., Capponi, G., Crispini, L., Di Vincenzo, G., Ghezzo, C., Meccheri, M. & Palmeri, R., 2003. Mafic rocks at the Wilson – Bowers Terrane transition and within the Bowers Terrane: implications for a geodynamic model of the Ross Orogeny. *Terra Antartica Reports*, **9,** 145–148.
Rubatto, D. & Hermann, J., 2001. Exhumation as fast as subduction? *Geology*, **29,** 3–6.
Sill, J. D., 1982. The retrogression of ultramafic granulites from the Scourian of NW Scotland. *Mineralogical Magazine*, **46,** 55–61.
Spalla, M. I., Lardeaux, J. M., Dal Piaz, G., Gosso, G. & Messiga, B., 1996. Tectonic significance of Alpine eclogites. *Journal of Geodynamics*, **21,** 257–285.
Spear, F. S., 1981. An experimental study of hornblende stability and compositional variability in amphibolite. *American Journal of Science*, **281,** 697–734.
Spear, F. R., 1993. *Metamorphic Phase Equilibria and Pressure-Temperature-Time Paths*. Mineralogical Society of America, Monograph, **1,** pp. 799. Washington, DC.
Talarico, F., Ghiribelli, B., Smith Siddoway, C., Palmeri, R. & Ricci, C. A., 1998. The northern Victoria Land segment of the Antarctic paleo-pacific margin of eastern Gondwana: new constraints from the Lanterman and Mountaineer Ranges. *Terra Antartica*, **5,** 245–252.
Taylor, W. R., 1998. An experimental test of some geothermometer and geobarometer formulations for upper mantle peridotites with application to the thermobarometry of fertile lherzolite and garnet websterite. *Neues Jahrbuch Mineralogie Abhandlunge*, **172,** 381–408.
Tsai, C. H., Liou, J. G. & Ernst, W. G., 2000. Petrological characterization and tectonic significance of retrogressed garnet peridotites, Raobazhai area, north Dabie Complex, east-central China. *Journal of Metamorphic Geology*, **18,** 181–192.
Wang, Z. & Ji, S., 2000. Diffusion creep of fine-grained garnetite: implications for the flow strength of subducting slabs. *Geophysical Research Letters*, **27,** 2333–2336.
Wilks, K. R. & Carter, N. L., 1990. Rheology of some continental lower crustal rocks. *Tectonophysics*, **182,** 57–77.
Wood, B. J., 1974. The solubility of alumina in orthopyroxene coexisting with garnet. *Contributions to Mineralogy and Petrology*, **46,** 1–15.
Zhang, R. Y., Liou, J. G. & Cong, B., 1994. Petrogenesis of garnet-bearing ultramafic rocks and associated eclogites in the Su-Lu ultrahigh-P metamorphic terrane, eastern China. *Journal of Metamorphic Geology*, **12,** 169–186.

*Received 5 April 2006; revision accepted 11 October 2006.*

© 2007 Blackwell Publishing Ltd